Research Square

Preprints are preliminary reports that have not undergone peer review.
They should not be considered conclusive, used to inform clinical practice,
or referenced by the media as validated information.

Single-Cell Transcriptomics Highlights Macrophage-Driven Regulation of EndMT and Repair in Injured Muscle

Silvia Brunelli

silvia.brunelli@unimib.it

University of Milano Bicocca https://orcid.org/0000-0003-1753-5346

Filipa Timóteo-Ferreira

University of Milano Bicocca https://orcid.org/0000-0002-9454-162X

Riccardo Gamberale

University of Milano Bicocca

Cristiana Barone

University of Milano Bicocca

Cristina D'Orlando

University of Milano Bicocca

Mauro Bergamaschi

University of Milano Bicocca

Anna Sofia Tascini

Raffaella Meneveri

Emanule Azzoni

Article

Keywords: Skeletal muscle regeneration, Endothelial cells, Macrophages, Endothelial-to-Mesenchymal transition, Inflammation

Posted Date: April 24th, 2025

DOI: https://doi.org/10.21203/rs.3.rs-6288736/v1

License: This work is licensed under a Creative Commons Attribution 4.0 International License.
Read Full License

Additional Declarations: There is **NO** Competing Interest.

Version of Record: A version of this preprint was published at Communications Biology on May 11th, 2026. See the published version at https://doi.org/10.1038/s42003-026-10194-z.

"Single-Cell Transcriptomics Highlights Macrophage-Driven Regulation of EndMT and Repair in Injured Muscle"

Filipa Timóteo-Ferreira[1], Riccardo Gamberale[1], Cristiana Barone[1], Cristina D'Orlando[1], Mauro Bergamaschi[1], Anna Sofia Tascini[2], Raffaella Meneveri[1], Emanuele Azzoni[1,3], Silvia Brunelli[1,3*]

[1] School of Medicine and Surgery, University of Milano-Bicocca, Monza, Italy
[2] Center for Omics Sciences, IRCCS Ospedale San Raffaele, Milano, Italy
[3] Fondazione IRCCS San Gerardo dei Tintori, Monza, Italy

*** Correspondence:**
Silvia Brunelli
silvia.brunelli@unimib.it

Keywords: Skeletal muscle regeneration, Endothelial cells, Macrophages, Endothelial-to-Mesenchymal transition, Inflammation

Abstract

Following muscle injury, a series of well-coordinated events ensure proper healing. Among these, inflammatory cells, particularly macrophages (MPs), play a fundamental role by phagocytosing damaged tissue and coordinating the actions of other cells involved in regeneration. Partial depletion of infiltrating MPs has been associated with endothelial cells (ECs) undergoing endothelial-to-mesenchymal transition (EndMT), contributing to extracellular matrix accumulation. However, the specific mechanisms linking MPs to this process, as well as their role in influencing EC fate, remain unclear. Here, we adopt a single cell transcriptomics approach in mice to define a specific signature of the regenerating muscle niche. We show that perturbing MP recruitment upon injury results in impaired MP polarization, creating an aberrant inflammatory, non-regenerative, and less angiogenic microenvironment which in turn drives ECs toward EndMT. Furthermore, we highlight complex signalling interactions between MPs and ECs, with SPP1 emerging as one of the critical modulators of these processes.

Introduction

The regeneration of skeletal muscle relies on a complex network of interactions between tissue-resident and recruited cells that develops across different regenerative stages. Following muscle injury, an inflammatory response is triggered, leading to the recruitment of blood-derived monocytes that differentiate into inflammatory macrophages (MPs) upon arrival to the damaged site (1). These inflammatory MPs secrete a variety of factors that prompt myogenesis and activate the surrounding muscle populations, collectively known as regenerating muscle niche (2). This niche supports and appropriately signals the healing process, being composed, among others, by muscle stem cells (MuSCs), which are the primary cells that differentiate into newly regenerated fibers; fibro-adipogenic progenitors (FAPs), mainly involved in extracellular matrix (ECM) turnover; and endothelial cells (ECs), responsible for tissue revascularization (3).

The success of the repair process depends on a timely and balanced transition from a pro-inflammatory to an anti-inflammatory/regenerative environment. This transition is primarily driven by the polarization of the existing MP population in the muscle. By the end of day 3 post-injury, the previously recruited MPs shift from an inflammatory towards an anti-inflammatory/regenerative phenotype (1, 4, 5), that is accompanied by a metabolic change from glycolysis to oxidative phosphorylation and glutamine metabolism (5, 6). In the event that this transition is disrupted by experimental or pathological factors, the secretion of cytokines and growth factors becomes imbalanced and the fate of MuSCs, FAPs and ECs is altered, ultimately leading to failed muscle regeneration and often fibrosis (4, 7, 8). Although FAPs are considered the main contributors to ECM deposition through their ability to differentiate into collagen-producing fibroblasts and/or adipocytes (7, 9, 10), recent research has highlighted that ECs can also contribute to fibrosis (8, 11, 12). A dysregulated inflammatory muscle environment can trigger endothelial-to-mesenchymal transition (EndMT), a process where ECs lose their endothelial function and phenotype and differentiate into ECM-producing mesenchymal cells (8, 11). Nonetheless, further research is required to fully elucidate the cellular and molecular mechanisms driving EndMT in the muscle, as well as the role of MPs in influencing this process.

In this study, we sought to elucidate the role of MPs in muscle regeneration by performing single-cell transcriptomics on the regenerating skeletal muscle niche. We focused on the crosstalk between MPs and ECs and its influence on ECs behaviour. We found that an impairment in MP recruitment dynamics leads to significant changes in the cellular composition of the regenerating muscle niche, with ECs suffering a transformation towards a mesenchymal phenotype via TGF-β signalling that ultimately jeopardizes both angiogenesis and myogenesis. In addition, we uncover SPP1 as a cytokine produced by MPs involved on the crosstalk with ECs and with impact on their phenotypic fate.

Results:

Single-cell RNA sequencing reveals that impaired macrophage recruitment after injury alters the cellular composition of the muscle regenerating niche

Cdh5-CreER^{T2} transgenic mice expressing a tamoxifen (TAM)-inducible form of Cre recombinase (*CRE-ER^{T2}*) under the control of the endothelial-specific gene VE-Cadherin (*Cdh5*) were crossed with *R26R-tdTomato* homozygous reporter mice. To obtain insight on the crosstalk between innate immune cells and vascular-associated cells *in vivo*, the transcriptome of the regenerating muscle niche of *Cdh5-CreER^{T2}:R26R-tdTomato* mice was analyzed after partial ablation of infiltrating MPs. To this purpose, Cre recombination was induced in *Cdh5-CreER^{T2}:R26R-tdTomato* mice with three consecutive subcutaneous (SC) injections of tamoxifen (TAM) at postnatal days 6,7 and 8. Thus, virtually all postnatal VE-Cadherin-expressing cells were labelled, allowing cellular tracking of ECs fate in the adult skeletal muscle. To deplete circulating monocytes and reduce MP infiltration, 60 days-old mice were intravenously injected with liposomes containing Clodronate (CLL) or PBS as control (SHAM). Intravenous injections of CLL were performed one day before and two days after cardiotoxin (CTX) damage on quadriceps muscles to ensure a steady MP depletion throughout regeneration. Based on our previous data, in these experimental conditions ECs are undergoing EndMT 5 days post-injury (8). Therefore, at this time point muscles were collected and processed for analysis. A total of 6 mice were employed and divided into the two experimental groups (**Supplementary Figure S1A**). To confirm an effective reduction of circulating monocytes in CLL vs SHAM treated mice, peripheral blood (PB) was collected 4 days after CTX injection. Flow cytometric analysis showed a significant depletion of CD45$^+$ CD11b$^+$/ F4/80$^+$ circulating phagocytes, which were less frequent in CLL-treated than in SHAM-treated animals (7.9 ± 0,5% vs 3.3 ± 0,2%, respectively, $P < 0.01$; **Supplementary Figure S1B**). Quadriceps muscles were then collected, dissociated into single-cell suspensions, processed on the Chromium platform (10x) and sequenced (Illumina). Seurat package was used for single-cell RNA-sequencing (scRNA-seq) data filtering and processing (see Materials and methods). After filtering, the scRNA-seq dataset contained 33,935 cells (SHAM= 18,336, CLL=15,599), expressing a total of 22,296 different genes. Experimental replicates generated from different mice (n = 3) presented only minor differences, most notably a variation in the incidence of mesenchymal population in the SHAM9 sample, suggesting that the datasets contained minimal batch effects and mouse-to-mouse variability (**Supplementary Figure S2A-D**). Therefore, for subsequent analyses, biological replicates were combined and integrated to improve cell sample size and statistical power.

Uniform manifold approximation and projection (UMAP) and t-distributed stochastic neighbour embedding (t-SNE) were used to visualize the embedding of the integrated scRNA-seq dataset

(**Figure 1A, 1C**). Unsupervised clustering resulted in 35 different clusters across the 6 samples. Clusters were next labelled and merged based on canonical skeletal muscle gene expression markers, obtaining a total of 14 (**Figure 1B)**. The top 5 marker genes of each cluster are shown in **Figure S2D**. MuSCs and myoblasts formed a cluster marked by the expression of *Pax7* and *Myod1*, while mature myocytes formed a distinct one expressing *Myh1* (myosin heavy chain 1) and *Acta1* (skeletal muscle alpha actin 1). ECs were marked by the expression of *Cdh5* (VE-Cadherin) and *Pecam1* (CD31), while a cluster of pericytes and smooth muscle cells expressed *Rgs5* and *Pdgfrb*. We were also able to identify a cluster marked by the expression of *Mpz* that corresponds to Schwann cells (neural) and another that expressed *Adipoc* and *Plin1* representing adipocytes. Immune cells formed several discrete clusters that represent the main immune populations described to be present 5 days post-injury (13). B, T and NK cells were grouped for simplicity and were marked by the expression of *Ptprc* (CD45), *Flt3* and *Ccl5*. Neutrophils were identified as expressing *S100a8* and *S100a9*. Mast cells by *Cpa3* and *Cma1* and dendritic cells were marked by the expression of *Cd209a* and *Cd74*. MPs formed the largest cluster of immune cells marked by *Adgre1* (F4/80), *Aif1* and *Csf1r* expression. In addition, a population of mesenchymal cells containing tenocytes expressing *Scx* and *Tnmd*, and FAPs expressing *Pdgfrα* formed another cluster. Interestingly, we were able to identify a cluster of cells recently described as immunomyoblasts (14) that expressed both immune (*C1qa, C1qb, H2-Eb1, H2-Aa*) and myogenic genes (*Pax7, Myf5*) (**Figure 1B, Supplementary Figure S2D**). The cell populations present in our experiment are consistent with previously published literature (13, 14), suggesting that our data recapitulates key events in skeletal muscle regeneration. Nonetheless, differences in cellular composition of the regenerating muscle niche were evident between mice treated with SHAM and those treated with CLL. As expected, CLL-treated mice showed a decrease in MPs (35.77% vs 15.26%). In addition, we also observed a near-twofold decline in ECs (10.68% vs 2.83%) and a concomitant increase in mesenchymal cells, mainly driven by FAPs (23.93% vs 58.16%) (**Figure 1D, Supplementary Figure S1C**).

The impact of an impaired muscle regenerating niche on MuSCs and FAPs

A delay in myogenesis resulting from the partial depletion of MPs in *Tibialis anterior* (TA) and triceps muscles was demonstrated in previously published data from our group, with histological analysis of muscles 5 days post injury already exhibiting differences in cellular organization and composition (8). Similar histological differences were consistently observed in cross sections of the quadriceps of CLL-treated mice (**Supplementary Figure S1D**) and align with the shifts observed in the cellular composition in our scRNA-seq dataset (**Figure 1D**).

Since MuSCs are primarily responsible for the development of new muscle fibers, we conducted sub-clustering on a total of 2,967 MuSCs to investigate potential alterations in their

subpopulations that could explain this delay in myogenesis. We identified three distinct clusters of MuSCs (**Figure 2A-B**), a quiescent subpopulation marked by *Pax7* expression, activated/dividing MuSCs expressing *Pax7, Myod1*, and *Cdk1*, and committed MuSCs marked by *Myog* expression (**Figure 2A**). All of them were negative for the mature myocyte marker *Myh1* (**Figure 2A).** The different MuSC states presented variations in proportions between our two experimental conditions, with CLL-treated mice showing a lower percentage of quiescent MuSCs (75.4% vs. 64.4%), higher percentage of activated MuSCs (9.8% vs. 17.8%), and a similar proportion of committed MuSCs (14.8% vs. 17.8%) (**Figure 2C**). These findings suggest that MP depletion results in a continuous activation of quiescent MuSCs, possibly due to aberrant signalling from the surrounding regenerative niche, which is essential for their commitment to myocytes or their return to the quiescent pool.

Next, we sought to understand the biological processes underlying the higher proportion of FAPs observed in the CLL condition. For this, we subjected the FAP population, consisting of a total of 13,837 cells (**Figure 2D**), to differential gene expression (DGE) analysis followed by gene set enrichment analysis (GSEA), querying the Gene Ontology (GO) Biological Process and KEGG databases. Recent studies have demonstrated that traditional scRNA-seq DGE methods display an inferior performance when compared to pseudo-bulk approaches in the presence of biological replicates, as they focus on individual cell differences and do not account for inter-individual variation (15, 16). Given that our experimental scheme included three biological replicates, and our focus is on the impact of our experimental condition rather than biological variability, we employed a pseudo-bulk approach using the DESeq2 package (**Table S1**).

GSEA results revealed that when MP recruitment is impaired, FAPs exhibit activation of the glycolytic and pentose phosphate pathways, indicating increased anabolic metabolism at this time point compared to normal regenerative conditions (**Figure 2E, Table S2**). The activation of carbon metabolism emphasizes an increased energy demand in FAPs under the CLL condition, while the activation of DNA replication sustains enhanced proliferative activity (**Figure 2E**). Indeed, a metabolic shift towards glycolysis is commonly associated with higher proliferation rates, as it provides a faster means of energy production, and is further supported by the activation of HIF-1 signalling (**Figure 2E)**, a pathway active under hypoxic conditions and described to promote glycolysis. Such metabolic state dysregulations have been equally observed in FAPs under pathological conditions, where it is linked to an increased fibrogenic potential (17), and under dystrophic conditions, where it correlates with higher FAPs proliferation and adipogenic differentiation rates (18).

In the CLL condition FAPs also display enhanced collagen biosynthesis, alongside suppression of inflammatory response and of endothelial cell proliferation/ angiogenesis regulation (**Figure**

2E). The suppression of Notch and Hedgehog signalling (**Figure 2E**) suggests similar higher FAP adipogenic differentiation, as these pathways have been proved to negatively regulate FAP proliferation and adipogenic differentiation both *in vitro* and *in vivo* (19, 20).

Together, these findings indicate that deficiency on MP recruitment dynamics affects the correct onset of repair and contributes to both the sustained activation and impaired resolution of FAPs, mirroring changes reported in dystrophic contexts.

Compromised MP infiltration contributes to ECs phenotypic switch and upregulation of TGF-β signalling pathway genes

Previous work from our group has demonstrated that compromised MP infiltration during skeletal muscle regeneration triggers ECs to undergo EndMT, contributing to the uncontrolled expansion of fibroblast/mesenchymal cells (8). However, ECs-specific transcriptional changes remained unexplored. To address this gap, DGE analysis (**Table S3)** was conducted on the EC subsets across experimental conditions, followed by GSEA analyses (**Table S4)**.

The GSEA analysis revealed that, in CLL-treated mice, ECs exhibit suppression of endothelial cell differentiation and angiogenesis (**Figure 3A**), as sustained by the consistent significant downregulation of key endothelial markers (*Cdh5, Pecam1, Vwf, Kdr,* and *Tie1*) across all sequenced biological samples (**Figure 3D**). In addition, the activation of Hippo signalling and the concurrent suppression of the Notch signalling pathway (**Figure 3A-B**) suggest altered angiogenesis. The activation of Hippo signalling in ECs inhibits the transcriptional coactivator YAP (Yes-associated protein 1). YAP, known for its influence on the expression of genes regulating cell proliferation, survival, and differentiation, plays a pivotal role in vasculogenesis and angiogenesis (21-23). On the other hand, Notch signalling is essential for vascular stabilization and differentiation of the emerging vascular tree by inhibiting ECs proliferation and promoting the stabilization of cell–cell junctions (24-26).

At the same time, ECs in CLL-treated regenerating muscles display activation of pathways associated with mesenchymal cell differentiation, fibroblast proliferation and ECM production (**Figure 3A**). This is related to the significant up-regulation of mesenchymal genes such as *Acta2* (αSMA), *Cdh2* (N-cadherin), *Fn1* (fibronectin), *S100A4* (FSP-1) and different collagen types (**Figure 3D**), with the presence of ECM-related genes among the top 20 significant DEGs (**Figure 3C**).

Immunostaining on muscle sections of *Cdh5-CreER^{T2}:R26R-tdTomato* mice confirmed the reduction in the EC population in CLL-treated mice in comparison to the control (822 ± 124 $CD31^+$ cells/mm^2 vs 511 ± 65 $CD31^+$ cells/mm^2, SHAM vs CLL respectively, P <0.0913, **Figure 3F, Supplementary Figure S3**). ECs exhibited different morphology and distribution patterns in

the two experimental conditions, being uniformly shaped and regularly distributed throughout the regenerative area in controls, whereas in CLL-treated animals their morphology was variegated and their distribution appeared irregular, occasionally clustering together resembling small niches (**Figure 3E and Supplementary Figure S3**). Interestingly, in the CLL-treated condition the lineage tracing label tdTomato was detected in a significantly higher subset of cells not marked by CD31 (15 ± 2 cells/mm^2 vs 92 ± 8 cells/mm^2, SHAM vs CLL respectively, P <0.001, **Figure 3F, Supplementary Figure S3**). Col1a1, the main component of fibrotic ECM and a significant upregulated gene on ECs DEG analysis (**Figure 3D),** showed a higher number of cells expressing this ECM protein in the immunostained muscles of CLL-treated mice (**Figure 3E)**, including both CD31$^+$ cells (75 ± 8 cells/mm^2 vs 131 ± 15 cells/mm^2, respectively, P <0.05, **Figure 3E and 3G**) and tdTomato$^+$ cells (17 ± 5 cells/mm^2 vs 64 ± 15 cells/mm^2, respectively, P <0.05, **Figure 3E and 3G**).

Another significant observation in this context is the activation of TGF-β signalling (**Figure 3A-B**), a pathway well-recognized as a driver of EndMT in various tissues and pathological conditions (27-29). This activation is evidenced by the significant upregulation of key TGF-β-associated transcription factors, including *Snai1*, *Twist1*, *Twist2*, and *Serpine1* (PAI-1), as well as increased expression of *TGF-β2* and *TGF-β3* isoforms (**Figure 3C**). Further corroborating the involvement of TGF-β signalling in skeletal muscle EndMT is the suppression of phosphatidylinositol signalling (**Figure 3B**), which is known to mediate angiogenesis and VEGF expression (30), and to inhibit TGF-β-induced EndMT in bone marrow-derived endothelial progenitor cells (31). These observations are consistent with our previously published finding, which demonstrated elevated TGF-β/SMAD signalling in endothelial-derived progenitors in the absence of MPs seven days post-injury (8).

Several genes - *Dll4, Pdgfb, Aplnr, Apln,* and *Osm* (**Figure 3D**) - known to play crucial roles in the interaction between myogenesis and angiogenesis (32-34) were found to be significantly downregulated in ECs from CLL-treated mice. These findings, combined with the observed reduction in quiescent MuSCs and concomitant increase in activated MuSCs (**Figure 2C**) suggest that disrupted crosstalk with ECs could hamper the ability of MuSCs to commit to myocyte differentiation and/or return to the quiescent pool (33). Furthermore, the suppression of immune and inflammatory responses (**Figure 3A**), implies that EC dysfunction similarly affects ECs and immune cells interaction.

Taken together, these findings suggest that MP depletion in regenerating muscles results in transcriptional and phenotypic alterations in ECs. The perturbation of MP recruitment triggers EndMT through TGF-β signalling pathway activation, which impairs ECs function. These

changes adversely affect the regenerative microenvironment by impairing angiogenesis, myogenesis and immune response, highlighting their interconnection during muscle repair.

Macrophages exhibit a dysregulated transcriptomic profile upon impaired recruitment following muscle injury

MPs are highly plastic cells with the ability to acquire different inflammatory phenotypes and functions depending on their origin and tissue microenvironment, expressing a specific gene signature representative of each specialized function during the different phases of muscle repair (5). To investigate MP heterogeneity between experimental conditions, we subjected the MP population, consisting of a total of 8,940 cells, to unsupervised clustering. This analysis revealed seven clusters (**Figure 4A**), which were subsequently merged and classified into four subtypes based on their top marker gene expression profile (**Figure 4B**).

The Inflammatory MP cluster was characterized by genes related to interferon signalling (*Ifitm3, Ifit3, Irf7, Ifit2*), commonly associated with pro-inflammatory activity. The ECM-related MP cluster expressed genes involved in collagen regulation and ECM remodelling (*Dcn, Col5a2, Serpinh1*). The Proliferating MP cluster exhibited genes linked to cell division, cytoskeletal dynamics, and intracellular transport (*Stmn1, Tubb5, Birc5, Tuba1b, Ran*). The predominant MP subtype identified expressed MHC II genes (*H2-Ab1, H2-Aa, H2-Eb1*) and typical M2 markers, including *Mrc1* (Cd206), *Cd163*, and *Gpnmb*, and was classified as M2-like MPs (**Figure 4C**). All clusters were positive for *Adgre1* (F4/80) and *Cx3cr1* and negative for dendritic cell markers *Flt3* and *Cd209a* (**Supplementary Figure S4A**) supporting their MP identity. These populations resembled MP subtypes recently described during skeletal muscle regeneration (35-37). A slight difference in MP composition was observed between conditions, with CLL-treated mice presenting a lower percentage of Inflammatory (3,92% vs 1,13%) and M2-like MPs (86,14% vs 79,21%) and a higher one of Proliferating (1,65% vs 7,18%) and ECM-related MPs (8,29% vs 12,47%) (**Figure 4C**).

Given the crucial role of M2-like MPs in orchestrating the regenerative process (2) to understand what underlying functions and mechanisms could be dysregulated and impacting the regenerative environment we conducted DGE and GSEA analysis within this subset (**Table S5, S6**).

Under normal repair conditions, at the observed time point, MPs should have already polarized towards an anti-inflammatory/pro-regenerative phenotype, characterized by oxidative phosphorylation and glutamine metabolism together with pro-angiogenic and reparative functions (5, 37). However, in CLL-treated mice, MPs displayed higher activation of pathways typically associated with a pro-inflammatory state, including glycolysis, HIF-1α pathway, and TNF signalling (**Figure 4F**). Furthermore, MPs in CLL mice presented an activation of cholesterol metabolic process and lipid biosynthetic process (**Figure 4F**).

Key genes associated with the anti-inflammatory and pro-regenerative response, including *Gdf15, Apoe, Selenop, Fos, Ccr5*, and *Igf2*, were significantly downregulated, whereas inflammatory genes such as *Ifnb1, Hp, Cxcl10, Tnf, Ccl2, Vim, Tgfbi*, and *Ltbp2* were significantly upregulated (Figure 4E). Although not statistically significant, well-established cytokines associated with MP inflammatory profile exhibited altered expression patterns. *Il1b* and *Cd86*, markers of inflammatory MPs, showed higher average expression in the CLL condition, as did *Tgfb1* and *Il10* - markers of anti-inflammatory MPs (38) (**Supplementary Figure S4B**). In addition, MP-derived *Igf1*, a factor crucial for resolving inflammation and driving MP polarization (39), was downregulated (**Supplementary Figure S4B**).

GO biological process analysis further indicated the suppression of immune response- and angiogenesis-related processes (**Figure 4F**) with *Vegf*, a fundamental cytokine produced by MPs to induce angiogenesis, exhibiting a significant downregulation (**Figure 4E**).

Taken together, these findings suggest that impaired MP recruitment during muscle regeneration disrupt MP polarization and sustain a pro-inflammatory state, which may in turn affect resolution of inflammation by impairing key regenerative processes such as angiogenesis, myogenesis, and ECM remodelling, ultimately compromising muscle repair and acting as a trigger on ECs phenotypic switch.

Interactions between Macrophage ligands and Endothelial cells receptors identifies intercellular communication influencing endothelial cells behaviour

The cytokines and growth factors released by MPs can prompt different cellular responses. Thus, to address the impact of dystrophic MPs on EC fate decisions, we conducted CellChat analysis focusing on secreted signalling where MPs served as sources and ECs as targets (**Table S7**).

The first striking observation was the presence of a higher number of interactions in the CLL condition compared to the control (**Figure 5A**). Among these interactions, TNF exhibited increased interaction probability (**Figure 5B, Supplementary Figure S5A**), consistent with results from DGE and GSEA analysis (**Figure 4E, F**). Moreover, interactions dependent on another cytokine, osteopontin (SPP1), were exclusively detected in the CLL condition (**Figure 5A, Supplementary Figure S5A**). Conversely, the interaction probability associated with growth differentiation factor 15 (GDF15), a gene previously identified as downregulated in the MP DGE analysis (**Figure 4E**), was reduced in CLL-treated mice compared to SHAM (**Figure 5B, Supplementary Figure S5A**). This was an interesting finding as recent literature describes SPP1 and TNF as pro-inflammatory cytokines involved in TGF-β signalling (40-42), while GDF15 has been recognized as a key MP-derived factor in orchestrating the pro-regenerative phase during muscle repair (43). Therefore, our results identified TNF, SPP1, and GDF15 as potential key

upstream signals driving MPs and ECs crosstalk during generation and hinted at their interaction with the TGF-β pathway at the onset of EndMT in the muscle.

The analysis of signalling pathway information flow across conditions revealed an enrichment of TGF-β, TNF, and SPP1, along with a reduction in GDF signalling in CLL-treated mice. These findings further suggest a compromised transition from a TNF-rich to a TGF-β-rich environment, characterized by overlapping cytokine signalling and the presence of a microenvironment with elevated pro-inflammatory signals and diminished regenerative cues (**Supplementary Figure S5B**).

To validate CellChat findings, we performed immunostaining for F4/80 and SPP1 (**Figure 5C**). We detected a reduced number of F4/80$^+$ cells in the CLL condition (1264 ± 257 cells/mm^2 vs 674 ± 81 cells/mm^2, SHAM vs CLL respectively, P <0.094, **Figure 5D)** while SPP1 expression displayed a broader distribution and a significantly higher proportion of SPP1$^+$ MPs in CLL-treated mice (29 ± 1% vs 50 ± 5%, SHAM vs CLL respectively, P <0.05, **Figure 5E**), thus aligning with our scRNA-seq results.

In addition to MPs, SPP1 protein expression was observed in non-MP cells (**Figure 5C**). Thus, we examined *Spp1* gene expression across the major cell populations in our scRNA-seq dataset. Consistently, CLL-treated mice showed elevated *Spp1* gene expression not only in MPs but also in FAPs, MuSCs, and ECs (**Figure 5F**) In contrast, under control condition, *Spp1* expression was restricted to MPs, MuSCs, and myocytes. Further analysis of signalling genes revealed that in CLL-treated mice, MPs, FAPs, MuSCs, ECs, and myocytes exhibited higher expression of TGF-β isoforms, particularly *Tgf-β2* and *Tgf-β3*, whereas *Tnf* and *Gdf15* expression remained exclusive to MPs. In ECs, CellChat analysis reported that SPP1 signalled through the receptor CD44 and integrin heterodimer receptors (ITGB1, ITGB5, and ITGAV) (**Figure 5B, Supplementary Figure S5A).** Besides the expression of *Itgb1*, the expression of all other SPP1 receptors was exclusively observed in the CLL condition (**Supplementary Figure S5C),** further emphasizing the potential negative influence of elevated SPP1 expression on EC behaviour during impaired MP recruitment conditions.

Overall, our data show that the pro-inflammatory state caused by reduced MP recruitment during muscle regeneration results in altered cytokine expression patterns and disruption in the MP-EC interactions, pointing to a key role of SPP1 and identifying potential regulatory mechanisms impacting ECs phenotypic fate.

TGF-β and SPP1 synergize to promote EndMT *in vitro*

Given the established roles of TGF-β and SPP1 in promoting fibrosis during muscular dystrophy, and to further investigate their link to EndMT (42, 44), we cultured mouse skeletal muscle ECs

(mECs) (44) with TGF-β and/or SPP1 during a period of 3 and 5 days (**Supplementary Figure S6A**).

TGF-β-treated mECs exhibited a clear morphological transition from the characteristic cuboidal shape observed in the control group (medium without TGF-β or SPP1) to a more elongated, spindle-like phenotype at both 3 days (**Supplementary Figure 6B**) and 5 days (**Figure 6A**). Gene expression analysis confirmed this phenotypic change, showing a significant decrease in the endothelial marker *Cd31*, along with an increase in the transitional EndMT marker *Snail*, *PAI-1*, and the mesenchymal marker *αSMA* in TGF-β-treated ECs at both time points (**Supplementary Figure 6C, Figure 6B**).

In contrast, treatment with SPP1 alone did not induce significant changes in cell morphology. However, a reduction in VE-Cadherin gene expression was observed at day 3 (**Supplementary Figure 6C)**, with a significant decrease compared to the control group at day 5 (**Figure 6B**). Interestingly, the combination of SPP1 and TGF-β yielded the most striking results. ECs treated with both factors displayed a morphological transition similar to that seen with TGF-β alone at 3 and 5 days (**Supplementary Figure 6C, Figure 6B**), but with significantly lower expression of *Cd31* and *VE-Cadherin* after 3 days and significantly higher expression of the transitional EndMT markers *Snai1* and *PAI-1* after 5 days of treatment (**Figure 6B**).

These findings further strengthen the evidence that TGF-β signalling plays a key role in EndMT within skeletal muscle. Moreover, they suggest that SPP1 alone can affect *VE-Cadherin* expression in ECs and, when combined with TGF-β, exert a synergistic effect that enhances the expression of transcription factors associated with EndMT. This highlights the role of SPP1 in mediating the crosstalk between MPs and ECs, thereby influencing EC phenotypic fate.

Discussion:

Following muscle injury, sequential and coordinated events unfold to ensure effective muscle healing. During this process, inflammatory cells, particularly MPs, play a fundamental role by contributing to the phagocytosis of damaged tissue and by providing the necessary signals that support the activation and function of other cell types (2). We have previously shown that infiltrating MPs restrict ECs phenotype and prevent the development of persistent tissue fibrosis during regeneration (8). In this study, to gain a comprehensive understanding of MP influence on cell-cell interactions, we conducted a scRNAseq transcriptomic analysis of the regenerating skeletal muscle niche 5-day post-injury in experimental conditions leading to a partially impaired MP recruitment. We found that disrupted MP recruitment dynamics led to significant changes in the cellular composition of the regenerating muscle niche, including an increased abundance of mesenchymal cells and a reduced presence of MPs and ECs, correlating with histological differences observed between muscle tissues. In this setting, ECs undergo a transition towards a

mesenchymal phenotype, compromising angiogenesis, disrupting crosstalk with immune and myogenic cells, and contributing to ECM deposition. Additionally, the diminished MP population in regenerating muscle exhibits dysregulated phenotypic profiles, with M2-like MPs displaying activation of pro-inflammatory pathways, including glycolytic metabolism, HIF-1α, and TNF signalling, while concurrently suppressing anti-inflammatory/pro-regenerative immune responses and angiogenesis. This suggests that proper MP recruitment is necessary for correct MP polarization during muscle regeneration, ensuring appropriate inflammatory environment and EC function. Furthermore, analysis of intercellular communication and immunostaining highlighted specific ligand-receptor interactions between MPs and ECs, particularly involving SPP1 and revealing complex signalling mechanisms influencing ECs behaviour.

The essential role of monocyte-derived MPs in skeletal muscle regeneration has been demonstrated through myeloid-cell depletion studies (8, 45, 46) and MP recruitment blockade via MCP-1/CCR2 receptor knockout models (47, 48). In these animals, a significant impairment in muscle regeneration is observed, characterized by delayed myogenesis and angiogenesis, excessive ECM deposition, and increased adipocyte populations (8, 45-48). The balance between pro- and anti-inflammatory/ pro-regenerative MPs, alongside their transition from a TNF-rich to a TGF-β1-rich microenvironment, has been identified as critical for proper muscle healing (4, 46) and FAPs dynamics (7). In dystrophic muscle environments, where the MP phenotypic switch is disrupted, a large subset of MPs simultaneously expresses TNF and TGF-β1, leading to a breakdown of the ordered inflammatory transition, triggering FAPs survival and muscle fibrosis (7). Consistent with this, we observed a correlation between higher FAP numbers and impaired MP inflammatory profiles. In addition, increased FAP abundance was associated with suppression of Notch and Hedgehog signalling and dysregulated metabolic profile, specifically anabolic metabolism activation. While the MP inflammatory transition is known to control FAP dynamics, we provide evidence that this proper polarization is also key for restricting EC phenotype and function during regeneration. Indeed, the correct expansion of $CD206^+$ MPs has been shown to be essential to prevent EndMT in the muscle (11).

The involvement of EndMT and the influence of TGF-β signalling in the pathogenesis of fibrotic diseases have been well documented (27-29, 49). In line with this, our findings revealed TGF-β signalling activation in ECs undergoing EndMT during impaired skeletal muscle regeneration. Elevated TGF-β levels in muscle, five days post-injury, has been previously reported where impaired MP recruitment was associated with increased EndMT (8). While MPs do not appear to be the primary source of TGF-β at this stage, the observed upregulation of TGF-β2 and TGF-β3 in FAPs, MuSCs, myocytes, and ECs in CLL-treated mice likely contribute to increased TGF-β levels in muscle. Therefore, these increased TGF-β levels together with higher MP-derived TNF expression drive the disruption of the inflammatory environment and commit ECs to a

mesenchymal fate. Our results additionally demonstrate that the onset of EndMT adversely impacts ECs function. Specifically, reductions in ECs population, disturbances in their distribution, morphology, and transcriptional signature patterns. These changes ultimately affect blood vessel formation and growth, as corroborated by the visualization of Hippo signalling activation and simultaneous suppression of the Notch pathway.

In addition, the onset of EndMT is coupled with the deregulation of other cross-signalling events involving SPP1. SPP1 is an inflammatory cytokine undetectable under homeostatic conditions, but that becomes strongly upregulated by MPs and myogenic cells following injury (50, 51). While SPP1 does not directly contribute to the structural integrity of the ECM, its ability to bind to many ECM molecules allows it to indirectly facilitate and alter important ECM component interactions. In the muscle, its expression supports the infiltration of neutrophils and MPs and the overall repair process (52). However, aberrant expression of SPP1 negatively impacts inflammation and fibrosis in different tissues (53, 54), including in dystrophin deficient muscles (44) where it is a key regulator of MP and FAP interactions to control FAP differentiation (36). Furthermore, the connection between TNF, SPP1, and TGF-β signalling is supported by previous evidence demonstrating that TNF cooperates with and enhances TGF-β-induced EndMT (40, 41). Meanwhile, in dystrophic muscles, SPP1 contributes to both TGF-β processing in fibroblasts and the skewing of MP polarization toward a pro-inflammatory phenotype (42, 55). Recent scRNA-seq studies further support our findings as it was identified, in Duchenne Muscular Dystrophy (DMD) muscles, a subset of capillary ECs with elevated expression of collagen-related genes and fibronectin. Further analysis revealed that the inducers of such changes were stromal cells and MP-secreted factors, specifically TGF-β, SPP1, TNF-α, and IL-β, which activated the TGF-β pathway in ECs and drove their dysregulation (56).

Albeit central orchestrators of angiogenesis, recent studies have elucidated another essential role played by ECs in the cellular and molecular crosstalk of the regenerating muscle niche. Compelling evidence shows that the loss of ECs' biochemical and phenotypic identity can exacerbate deficits in myogenesis and angiogenesis under dystrophic conditions. Muscles from both DMD mice and patients exhibit cells expressing simultaneously mesenchymal and endothelial markers, with increased collagen deposition and fibronectin observed around capillaries (12, 56). ECs and MuSCs proliferate simultaneously after injury, with the coordination between angiogenesis and myogenesis being indispensable for the full restoration of skeletal muscle, a process stimulated by restorative MPs (33). Furthermore, both *in vitro* and *in vivo* studies have revealed an important function of ECs in regulating SC quiescence and self-renewal. This regulation is facilitated by MuSCs secretion of VEGF-A, which attracts ECs to form a vascular niche. Within this niche, ECs express Dll4, activating the Notch signaling pathway in SCs and promoting their quiescence (57). Interestingly, our results demonstrated both a

dysregulation of immune signaling and key factors involved in EC-MuSC crosstalk. In fact, Dll4 appeared as one of the downregulated EC genes, correlating with an increased activated MuSC population and a reduced presence of quiescent MuSCs in the regenerating niche of CCL-treated mice. We hypothesize that dysregulated Dll4 signaling may underlie continued MuSC activation, due to the lack of signals required for their return to the quiescent pool. This, in turn, could ultimately impact myogenesis. Further studies are required to investigate this connection.

These combined findings support the hypothesis that a temporally sequenced integration of inflammatory, angiogenic and myogenic events is crucial for skeletal muscle regeneration. This study also emphasizes that proper MP polarization and cytokine expression, particularly TGF-β, TNF and SPP1, is crucial for maintaining EC integrity and a successful healing process. Therefore, addressing the role of ECs and EndMT in muscular dystrophic conditions and age-related changes could represent a potential field of therapeutic interest.

Materials and methods

Mice

The mouse strains used in this study have been previously described (58, 59). A specific lineage tracing mouse model - *Cdh5-CreER^{T2}:R26R-tdTomato* – was employed for the *in vivo* studies on EndMT. Homozygous transgenic mice expressing a tamoxifen (TAM)-inducible form of Cre recombinase (*CRE-ER^{T2}*) under the control of the endothelial-specific gene VE-Cadherin (*Cdh5*) were crossed with *R26R-tdTomato* homozygous reporter mice. Cre recombination was then induced in double transgenic mice at postnatal days 6-7-8 with three subcutaneous (SC) injections of 25 µl TAM at 10 mg/ml (Sigma-Aldrich, St. Louis).

All animal procedures were performed at San Raffaele Scientific Institute animal facilities in accordance with European Union guidelines and with the approval of the Institutional Ethical Committee and Ministry of Health (Authorization 244/2020-PR). Mice were kept under controlled conditions (12h light/dark cycle and room temperature at 22 °C) and had free access to tap water and standard mice chow.

Muscle injury

For muscle injury experiments, 8-9 weeks-old mice were anesthetized with isoflurane and quadriceps muscle was injected with cardiotoxin (Latoxan) at 10 µM (100 µl per muscle) to induce muscle injury followed by regeneration. Muscles were then collected and processed for analysis 5 days after. For histology and immunofluorescence studies, muscles were collected and directly frozen in isopentane cooled in liquid nitrogen and stored at -80°C.

Depletion of circulating monocytes

8-9 weeks-old *Cdh5-CreER^{T2}:R26R-tdTomato* mice were intravenously injected (tail veins) with 200 µl liposomes containing Clodronate (CLL) - to deplete blood circulating monocytes and compromise macrophage recruitment to the site of injury - or 200 µl PBS liposomes as control (SHAM). CLL and SHAM injections were performed one day before and two days after acute damage induction by cardiotoxin on quadriceps. CLL and SHAM liposomes were purchased from:

http://www.clodronateliposomes.org/ashwindigital.asp?docid=26.

To confirm an effective reduction of circulating monocytes in CLL vs SHAM treated mice, blood was collected 4 days after cardiotoxin injection and processed for FACS analysis. Briefly, samples were stained and analysed in CMF (Calcium/Magnesium-Free PBS, 10% FBS, 5% Pen/Strep, 2 mM EDTA), incubated for 15 min with 0.5 mg/mL Fc block (1:500) (BD Biosciences, Franklin Lakes, NJ, USA) and labelled with a combination of PE-conjugated rat anti-CD45 (1:400) (BD Biosciences), PE-Cy7-conjugated rat anti-CD11b (1:200) (BD Biosciences) and APC-conjugated rat anti-F4/80 (1:200) (BD Biosciences). Appropriate fluorescence gating parameters were established with compensation beads (BD Biosciences), unstained, and fluorescence-minus-one (FMO) staining. In all of the samples, doublets were gated out using pulse geometry gates (FSC-H versus FSC-A and SSC-H versus SSC-A), whereas dead cells were excluded using Hoechst 33258 (Hellobio, Bristol, UK). Suspensions were analyzed using a Fortessa X-20 analyzer (BD Biosciences) and FlowJo software v10 (FlowJo/BD, Ashland, OR, USA).

Cell isolation from skeletal muscle

In brief, freshly isolated quadriceps were minced into small pieces and enzymatically dissociated with 1.5mg/mL Dispase (Gibco, 17105-041) and 0.12% (w/v) Collagenase type I (Sigma-Aldrich, C0130) in two cycles of 30min at 37°C under constant 240 rpm agitation. The suspension was then passed through a 16G needle, followed by a 26G needle and filtered through a 40µm sterile strainer. Then cold CMF was added to inactivate enzymes and red blood cells lysed. To remove cell debris from the suspensions, Ficoll separation was performed. Cells were resuspended in 7 mL of pre-warmed DMEM High Glucose (Gibco, 41965-039) supplemented with 10% FBS (Gibco, 10270-106), in a 15 mL falcon, and 3.5 mL of Ficoll slowly layered on top. Samples were centrifuged at 300g for 30 minutes with no brake nor acceleration and the cell layer formed aspirated to another falcon and washed with cell medium.

scRNA-seq

After obtaining a clean single-cell suspension, samples were processed on the Chromium platform (10×) using the Chromium Single Cell 3′ Library & Gel Bead Kit v3 kit (10×). After quality controls and quantification on TapeStation instrument (Agilent), libraries were sequenced on

NextSeq500 platforms (Illumina) generating around 100, 000 reads/cell. Raw sequencing data was demultiplexed with the mkfastq application (Cell Ranger v.3.0.2). Reads were aligned to the reference genome and assigned to genes with cellranger count (Cell Ranger v.3.0.2, genome: refdata-gex-mm10-2020-A), with the expect-cells option set to 10,000. The produced filtered matrixes were used for further bioinformatic analysis on R.

scRNA-seq data analysis

Seurat 4.3.0.1 (60) was used to analyse scRNA-seq data. All samples were filtered for quality control parameters (cells with more than 8% reads mapping to mitochondrial genes, feature counts greater than 7000 and smaller 350 and cells with less than 1000 transcripts were filtered out) and DoubletFinder (61) function performed. Applying these filters eliminated dying cells and doublets. Data was then normalized, scaled and dimensionality reduction performed through Principal Component Analysis (PCA) following Seurat's tutorial as evaluated by elbow plots. Cells from all samples were combined and batch correction executed using Harmony (62) (version 1.1), and unsupervised clustering performed. UMAP embedding parameters were based on the top 75 PCs and 0.9 dimensions for visualization. Each cluster was labelled based on canonical skeletal muscle gene expression. Differential expression analysis between conditions was conducted using DESeq2 (version 1.44.0). For each comparison, log2 (fold change) results were shrunken using the apeglm (63) package (version 1.26.1) to remove noise (differentially expressed genes with low counts and/or high dispersion values) while preserving significant differences.

Gene Set Enrichment Analysis (GSEA)

Gene Set Enrichment analysis (GSEA) was conducted using differentially expressed genes (DEG) evaluated by the DEseq2 package. All genes were ranked according to the log2FoldChange and GSEA analysis carried out using R package ClusterProfiler (64) (version 4.12.6) querying the Gene Ontology (GO) and KEGG database. The analysis was performed by setting the minimum gene set to 10 and maximum to 800. GO and KEGG terms were considered significant with a selected cutoff p-value of 0.05.

Immunofluorescence

Serial 10 µm thick muscle sections were sectioned on a cryostat (Leica CM 3050S), collected on Superfrost microslides (VWR) and stored at -80°C until analysis. For immunofluorescence muscle cryosections were thawed and fixed with 4% PFA in PBS for 10 minutes. Slides were then washed with PBS and permeabilized with 0.2% Triton and 1% BSA solution in PBS for 30 min, at RT. After, slides were blocked in 10% Donkey serum (DS) and 1% BSA solution in PBS, for 30 min, and then incubated with primary antibodies (Table I) in 1% DS in PBS overnight, in

a wet chamber, at 4 °C. The following day, slides were washed in PBS and incubated with secondary antibodies (Table I) in 1% DS in PBS for 1 hour at RT. Then, they were washed again, counterstained and mounted (Fluoroshield™ with 4',6-diamidino-2-phenyl-indole (DAPI), Sigma-Aldrich, F6057). Slides were examined and images were recorded under a confocal microscope Zeiss 710 equipped with an EC Plan-Neofluar 40x/1.30 Oil DIC M27. A minimum of 3 animals per group was used and at least 3 different fields per animal acquired. Counts from all fields corresponding to one animal were averaged. For quantification of cell numbers per field, individual cells were manually counted using the appropriate channels in combination with DAPI to identify nuclei on the software Fiji/ImageJ.

Table I – List of antibodies and concentrations

Antibody			Concentration
RFP	Rabbit	600-401-379 Rockland	1:400
RFP	Chicken	600-901-379 Rockland	1:100
CD31	Goat α-mouse	AF3628 R&D Systems	1:200
F4/80	Rat α-mouse	MCA497 Bio-Rad	1:100
Col1a1	Rabbit α-mouse	PA529569 Invitrogen	1:200
SPP1	Rabbit α-mouse	PA5-141129 Invitrogen	1:100
Alexa Fluor 568	Donkey α-rat	A78946 Invitrogen	1:500
Alexa Fluor 488	Donkey α-chicken	A78948 Invitrogen	1:500
Alexa Fluor 488	Donkey α-rabbit	A32790 Invitrogen	1:500
Alexa Fluor 555	Donkey α-rabbit	A32794 Invitrogen	1:500
Alexa Fluor 647	Donkey α-goat	A32849 Invitrogen	1:500
Alexa Fluor 555	Donkey α-goat	A32816 Invitrogen	1:500

Cell culture

Mouse endothelial cells previously isolated from skeletal muscle (65) were seeded at a density of 3125 cells/cm2, in 6 well culture plates (ThermoFisher Scientific, USA) coated with 0.1% Gelatin (Merck, G1393). Cells were cultured in DMEM High Glucose (Gibco, 41965-039) supplemented with 10% FBS (Gibco, 10270-106), 1% Pen Strep (Gibco, 15140-122), 1% L- Glutamine (Gibco, 25030-024) and 10 ng/mL of VEGF (Cell Signalling, 5211SF) for 24h. After this, mECs were switched to starvation (2% FBS) for another 24h. At the end of this period, mECs were cultured in the same starvation medium with or without 10 ng/mL of TGF-β1 (Cell Signalling, 5231LC), 100 or 200 ng/mL of SPP1 (R&D Systems, 441-OP-050), or 500 ng/mL of GDF-15 (R&D

Systems, 8944-GD-025) for 3 and 5 days. Then, cells were collected, and gene expression assessed by rt-qPCR analysis.

RNA extraction and cDNA synthesis

Total RNA from mECs was isolated using ReliaPrep RNA Cell Miniprep System (Z6011; Promega, Milan, Italy), following manufacturer instructions. Total RNA was quantified by measuring the absorbance at 260 nm in a Nanodrop (Thermofisher Scientific) and RNA purity was evaluated by the ratio of absorbance at 260 and 280 nm. RNA samples were reverse transcribed to cDNA with the LunaScript RT SuperMix Kit (E3010L) from New England Biolabs, using the Thermocycler 2027 (Applied Biosystems).

Real-time rt-qPCR analysis

Real-time rt-qPCR was carried out using the Luna Universal qPCR Master Mix (M3003X, New England Biolabs) and specific primers (Table II) in a QuantStudio™ 7 Flex Real-Time PCR System (Applied Biosystems). Amplification reactions were performed in duplicate. To check specificity, a dissociation curve was derived at the end of each run. Controls lacking reverse transcriptase were included to ensure no genomic DNA contamination during preparations. Results were normalized to GAPDH expression.

Table II – List of primer sequences

Primers		**Sequence**
GAPDH	Fwd	5' AACTTTGGCATTGTGGAAGG 3'
	Rev	5' ACACATTGGGGGTAGGAACA 3'
CD31	Fwd	5′-AGGGGACCAGCTGCACATTAGG-3′
	Rev	5′-AGGCCGCTTCTCTTGACCACTT-3′
VE-CAD	Fwd	5′-GTACAGCATCATGCAGGGCG-3′
	Rev	5′-ATTCGTATCGGATAGTGGGG-3′
αSMA	Fwd	5′-TCACCATTGGAAACGAACG-3′
	Rev	5′-ATAGGTGGTTTCGTGGATGC-3′
SNAIL1	Fwd	5′-CCACTGCAACCGTGCTTTT-3′
	Rev	5′-ATGTCCTTGCTCCACAAGCAC-3′
Col1a1	Fwd	5′-GGTATGCTTGATCTGTATCTGC-3′
	Rev	5′-AGTCCAGTTCTTCATTGCATT-3′
PAI-1	Fwd	5′-TCCTCCACAGCCTTTGTCAT-3′
	Rev	5′-ACATCTCCACTTTCGTCCCA-3′

Statistical analysis

Differences between the two experimental groups were compared by Student's t-test using GraphPad Prism 8. Statistical significance was accepted for comparisons where $p<0.05$. Values are presented as means ± S.E.M.

Data Availability Statement

The single-cell RNA sequencing data generated in this study have been deposited in the GEO database under accession code GSE291782.

Conflict of Interest

The authors declare that the research was conducted in the absence of any commercial or financial relationships that could be construed as a potential conflict of interest.

Author contributions

FTF: Conceptualization, Formal analysis, Investigation, Methodology, Project administration; Software, Visualization, Writing – original draft; RG: Investigation; CB: Investigation; MB: Investigation; AST: Software; RM: Resources; EA: Resources,; Funding acquisition; Methodology; Writing – review & editing ; SB: Conceptualization; Funding acquisition; Project administration; Resources; Supervision; Writing – review & editing.

Funding

The work was supported by the European Union's Horizon 2020 research and innovation program under the Marie Skłodowska-Curie grant agreement No 860034 to SB and FTF; Italian Ministry of Education-University-Research (2022TR9N4R to SB); Fondazione Cariplo "Biomedical Research conducted by young researchers" (2018-0102 to EA); Cariplo Telethon Alliance (GJC22013 to EA); Italian Ministry of Education-University-Research (2022TT8Z3M and P20223HEZC to EA); CB was supported by Fondazione Umberto Veronesi.

Acknowledgments

We kindly acknowledge the contributions of the personnel of the animal facilities and the Center for Omics Sciences (COSR) at the IRCCS Ospedale San Raffaele for technical support.

Bibliography

1. Varga T, Mounier R, Gogolak P, Poliska S, Chazaud B, Nagy L. Tissue LyC6- macrophages are generated in the absence of circulating LyC6- monocytes and Nur77 in a model of muscle regeneration. J Immunol. 2013;191(11):5695-701.
2. Chazaud B. Inflammation and Skeletal Muscle Regeneration: Leave It to the Macrophages! Trends in Immunology. 2020;41(6):481-92.
3. Wosczyna MN, Rando TA. A Muscle Stem Cell Support Group: Coordinated Cellular Responses in Muscle Regeneration. Developmental Cell. 2018;46(2):135-43.

4. Saclier M, Yacoub-Youssef H, Mackey AL, Arnold L, Ardjoune H, Magnan M, et al. Differentially activated macrophages orchestrate myogenic precursor cell fate during human skeletal muscle regeneration. Stem Cells. 2013;31(2):384-96.
5. Varga T, Mounier R, Horvath A, Cuvellier S, Dumont F, Poliska S, et al. Highly Dynamic Transcriptional Signature of Distinct Macrophage Subsets during Sterile Inflammation, Resolution, and Tissue Repair. The Journal of Immunology. 2016;196(11):4771-82.
6. Juban G, Chazaud B. Metabolic regulation of macrophages during tissue repair: insights from skeletal muscle regeneration. FEBS Lett. 2017;591(19):3007-21.
7. Lemos DR, Babaeijandaghi F, Low M, Chang CK, Lee ST, Fiore D, et al. Nilotinib reduces muscle fibrosis in chronic muscle injury by promoting TNF-mediated apoptosis of fibro/adipogenic progenitors. Nat Med. 2015;21(7):786-94.
8. Zordan P, Rigamonti E, Freudenberg K, Conti V, Azzoni E, Rovere-Querini P, et al. Macrophages commit postnatal endothelium-derived progenitors to angiogenesis and restrict endothelial to mesenchymal transition during muscle regeneration. Cell Death Dis. 2014;5(1):e1031.
9. Uezumi A, Fukada S, Yamamoto N, Ikemoto-Uezumi M, Nakatani M, Morita M, et al. Identification and characterization of PDGFRα+ mesenchymal progenitors in human skeletal muscle. Cell Death Dis. 2014;5(4):e1186.
10. Wosczyna MN, Konishi CT, Perez Carbajal EE, Wang TT, Walsh RA, Gan Q, et al. Mesenchymal Stromal Cells Are Required for Regeneration and Homeostatic Maintenance of Skeletal Muscle. Cell Rep. 2019;27(7):2029-35.e5.
11. Iavarone F, Guardiola O, Scagliola A, Andolfi G, Esposito F, Serrano A, et al. Cripto shapes macrophage plasticity and restricts EndMT in injured and diseased skeletal muscle. EMBO Rep. 2020;21(4):e49075.
12. Pessina P, Kharraz Y, Jardí M, Fukada S, Serrano AL, Perdiguero E, et al. Fibrogenic Cell Plasticity Blunts Tissue Regeneration and Aggravates Muscular Dystrophy. Stem Cell Reports. 2015;4(6):1046-60.
13. De Micheli AJ, Laurilliard EJ, Heinke CL, Ravichandran H, Fraczek P, Soueid-Baumgarten S, et al. Single-Cell Analysis of the Muscle Stem Cell Hierarchy Identifies Heterotypic Communication Signals Involved in Skeletal Muscle Regeneration. Cell Rep. 2020;30(10):3583-95.e5.
14. Oprescu SN, Yue F, Qiu J, Brito LF, Kuang S. Temporal Dynamics and Heterogeneity of Cell Populations during Skeletal Muscle Regeneration. iScience. 2020;23(4):100993.
15. Murphy AE, Skene NG. A balanced measure shows superior performance of pseudobulk methods in single-cell RNA-sequencing analysis. Nature Communications. 2022;13(1):7851.
16. Squair JW, Gautier M, Kathe C, Anderson MA, James ND, Hutson TH, et al. Confronting false discoveries in single-cell differential expression. Nature Communications. 2021;12(1):5692.
17. Farup J, Just J, de Paoli F, Lin L, Jensen JB, Billeskov T, et al. Human skeletal muscle CD90(+) fibro-adipogenic progenitors are associated with muscle degeneration in type 2 diabetic patients. Cell Metab. 2021;33(11):2201-14.e11.
18. Reggio A, Rosina M, Krahmer N, Palma A, Petrilli LL, Maiolatesi G, et al. Metabolic reprogramming of fibro/adipogenic progenitors facilitates muscle regeneration. Life Sci Alliance. 2020;3(3).
19. Marinkovic M, Fuoco C, Sacco F, Cerquone Perpetuini A, Giuliani G, Micarelli E, et al. Fibro-adipogenic progenitors of dystrophic mice are insensitive to NOTCH regulation of adipogenesis. Life Sci Alliance. 2019;2(3).
20. Kopinke D, Roberson EC, Reiter JF. Ciliary Hedgehog Signaling Restricts Injury-Induced Adipogenesis. Cell. 2017;170(2):340-51.e12.
21. Feng Y, Zou R, Zhang X, Shen M, Chen X, Wang J, et al. YAP promotes ocular neovascularization by modifying PFKFB3-driven endothelial glycolysis. Angiogenesis. 2021;24(3):489-504.
22. Kim J, Kim YH, Kim J, Park DY, Bae H, Lee DH, et al. YAP/TAZ regulates sprouting angiogenesis and vascular barrier maturation. J Clin Invest. 2017;127(9):3441-61.

23. Wang X, Freire Valls A, Schermann G, Shen Y, Moya IM, Castro L, et al. YAP/TAZ Orchestrate VEGF Signaling during Developmental Angiogenesis. Dev Cell. 2017;42(5):462-78.e7.
24. Mack JJ, Mosqueiro TS, Archer BJ, Jones WM, Sunshine H, Faas GC, et al. NOTCH1 is a mechanosensor in adult arteries. Nat Commun. 2017;8(1):1620.
25. Blanco R, Gerhardt H. VEGF and Notch in tip and stalk cell selection. Cold Spring Harb Perspect Med. 2013;3(1):a006569.
26. Ehling M, Adams S, Benedito R, Adams RH. Notch controls retinal blood vessel maturation and quiescence. Development. 2013;140(14):3051-61.
27. Cooley BC, Nevado J, Mellad J, Yang D, St. Hilaire C, Negro A, et al. TGF-β Signaling Mediates Endothelial-to-Mesenchymal Transition (EndMT) During Vein Graft Remodeling. Science Translational Medicine. 2014;6(227):227ra34-ra34.
28. Hashimoto N, Phan SH, Imaizumi K, Matsuo M, Nakashima H, Kawabe T, et al. Endothelial-mesenchymal transition in bleomycin-induced pulmonary fibrosis. Am J Respir Cell Mol Biol. 2010;43(2):161-72.
29. Zeisberg EM, Tarnavski O, Zeisberg M, Dorfman AL, McMullen JR, Gustafsson E, et al. Endothelial-to-mesenchymal transition contributes to cardiac fibrosis. Nat Med. 2007;13(8):952-61.
30. Kawasaki K, Smith Jr RS, Hsieh C-M, Sun J, Chao J, Liao JK. Activation of the Phosphatidylinositol 3-Kinase/Protein Kinase Akt Pathway Mediates Nitric Oxide-Induced Endothelial Cell Migration and Angiogenesis. Molecular and Cellular Biology. 2003;23(16):5726-37.
31. Zhang Z, Zhang T, Zhou Y, Wei X, Zhu J, Zhang J, et al. Activated phosphatidylinositol 3-kinase/Akt inhibits the transition of endothelial progenitor cells to mesenchymal cells by regulating the forkhead box subgroup O-3a signaling. Cell Physiol Biochem. 2015;35(4):1643-53.
32. Lee U, Stuelsatz P, Karaz S, McKellar DW, Russeil J, Deak M, et al. A Tead1-Apelin axis directs paracrine communication from myogenic to endothelial cells in skeletal muscle. iScience. 2022;25(7):104589.
33. Latroche C, Weiss-Gayet M, Muller L, Gitiaux C, Leblanc P, Liot S, et al. Coupling between Myogenesis and Angiogenesis during Skeletal Muscle Regeneration Is Stimulated by Restorative Macrophages. Stem Cell Reports. 2017;9(6):2018-33.
34. Christov C, Chrétien F, Abou-Khalil R, Bassez G, Vallet G, Authier FJ, et al. Muscle satellite cells and endothelial cells: close neighbors and privileged partners. Mol Biol Cell. 2007;18(4):1397-409.
35. Patsalos A, Halasz L, Oleksak D, Wei X, Nagy G, Tzerpos P, et al. Spatiotemporal transcriptomic mapping of regenerative inflammation in skeletal muscle reveals a dynamic multilayered tissue architecture. J Clin Invest. 2024;134(20).
36. Coulis G, Jaime D, Guerrero-Juarez C, Kastenschmidt JM, Farahat PK, Nguyen Q, et al. Single-cell and spatial transcriptomics identify a macrophage population associated with skeletal muscle fibrosis. Science Advances. 2023;9(27):eadd9984.
37. Sousa NS, Bica M, Brás MF, Sousa AC, Antunes IB, Encarnação IA, et al. The immune landscape of murine skeletal muscle regeneration and aging. Cell Rep. 2024;43(11):114975.
38. Arnold L, Henry A, Poron F, Baba-Amer Y, van Rooijen N, Plonquet A, et al. Inflammatory monocytes recruited after skeletal muscle injury switch into antiinflammatory macrophages to support myogenesis. J Exp Med. 2007;204(5):1057-69.
39. Tonkin J, Temmerman L, Sampson RD, Gallego-Colon E, Barberi L, Bilbao D, et al. Monocyte/Macrophage-derived IGF-1 Orchestrates Murine Skeletal Muscle Regeneration and Modulates Autocrine Polarization. Mol Ther. 2015;23(7):1189-200.
40. Yoshimatsu Y, Wakabayashi I, Kimuro S, Takahashi N, Takahashi K, Kobayashi M, et al. TNF-α enhances TGF-β-induced endothelial-to-mesenchymal transition via TGF-β signal augmentation. Cancer Sci. 2020;111(7):2385-99.
41. Yoshimatsu Y, Kimuro S, Pauty J, Takagaki K, Nomiyama S, Inagawa A, et al. TGF-beta and TNF-alpha cooperatively induce mesenchymal transition of lymphatic endothelial cells via activation of Activin signals. PLOS ONE. 2020;15(5):e0232356.

42. Kramerova I, Kumagai-Cresse C, Ermolova N, Mokhonova E, Marinov M, Capote J, et al. Spp1 (osteopontin) promotes TGFβ processing in fibroblasts of dystrophin-deficient muscles through matrix metalloproteinases. Human Molecular Genetics. 2019;28(20):3431-42.
43. Patsalos A, Halasz L, Medina-Serpas MA, Berger WK, Daniel B, Tzerpos P, et al. A growth factor-expressing macrophage subpopulation orchestrates regenerative inflammation via GDF-15. J Exp Med. 2022;219(1).
44. Vetrone SA, Montecino-Rodriguez E, Kudryashova E, Kramerova I, Hoffman EP, Liu SD, et al. Osteopontin promotes fibrosis in dystrophic mouse muscle by modulating immune cell subsets and intramuscular TGF-beta. J Clin Invest. 2009;119(6):1583-94.
45. Summan M, Warren GL, Mercer RR, Chapman R, Hulderman T, Rooijen NV, et al. Macrophages and skeletal muscle regeneration: a clodronate-containing liposome depletion study. American Journal of Physiology-Regulatory, Integrative and Comparative Physiology. 2006;290(6):R1488-R95.
46. Wang H, Melton DW, Porter L, Sarwar ZU, McManus LM, Shireman PK. Altered Macrophage Phenotype Transition Impairs Skeletal Muscle Regeneration. The American Journal of Pathology. 2014;184(4):1167-84.
47. Martinez CO, McHale MJ, Wells JT, Ochoa O, Michalek JE, McManus LM, et al. Regulation of skeletal muscle regeneration by CCR2-activating chemokines is directly related to macrophage recruitment. American Journal of Physiology-Regulatory, Integrative and Comparative Physiology. 2010;299(3):R832-R42.
48. Ochoa O, Sun D, Reyes-Reyna SM, Waite LL, Michalek JE, McManus LM, et al. Delayed angiogenesis and VEGF production in CCR2−/− mice during impaired skeletal muscle regeneration. American Journal of Physiology-Regulatory, Integrative and Comparative Physiology. 2007;293(2):R651-R61.
49. Pardali E, Sanchez-Duffhues G, Gomez-Puerto MC, Ten Dijke P. TGF-β-Induced Endothelial-Mesenchymal Transition in Fibrotic Diseases. Int J Mol Sci. 2017;18(10).
50. Uaesoontrachoon K, Wasgewatte Wijesinghe DK, Mackie EJ, Pagel CN. Osteopontin deficiency delays inflammatory infiltration and the onset of muscle regeneration in a mouse model of muscle injury. Dis Model Mech. 2013;6(1):197-205.
51. Hirata A, Masuda S, Tamura T, Kai K, Ojima K, Fukase A, et al. Expression profiling of cytokines and related genes in regenerating skeletal muscle after cardiotoxin injection: a role for osteopontin. Am J Pathol. 2003;163(1):203-15.
52. Wasgewatte Wijesinghe DK, Mackie EJ, Pagel CN. Normal inflammation and regeneration of muscle following injury require osteopontin from both muscle and non-muscle cells. Skeletal Muscle. 2019;9(1):6.
53. Freiholtz D, Bergman O, Pradhananga S, Lång K, Poujade F-A, Granath C, et al. SPP1/osteopontin: a driver of fibrosis and inflammation in degenerative ascending aortic aneurysm? Journal of Molecular Medicine. 2023;101(10):1323-33.
54. Oh K, Seo MW, Kim YW, Lee DS. Osteopontin Potentiates Pulmonary Inflammation and Fibrosis by Modulating IL-17/IFN-γ-secreting T-cell Ratios in Bleomycin-treated Mice. Immune Netw. 2015;15(3):142-9.
55. Capote J, Kramerova I, Martinez L, Vetrone S, Barton ER, Sweeney HL, et al. Osteopontin ablation ameliorates muscular dystrophy by shifting macrophages to a pro-regenerative phenotype. J Cell Biol. 2016;213(2):275-88.
56. Saleh KK, Xi H, Switzler C, Skuratovsky E, Romero MA, Chien P, et al. Single cell sequencing maps skeletal muscle cellular diversity as disease severity increases in dystrophic mouse models. iScience. 2022;25(11):105415.
57. Verma M, Asakura Y, Murakonda BSR, Pengo T, Latroche C, Chazaud B, et al. Muscle Satellite Cell Cross-Talk with a Vascular Niche Maintains Quiescence via VEGF and Notch Signaling. Cell Stem Cell. 2018;23(4):530-43.e9.
58. Wang Y, Nakayama M, Pitulescu ME, Schmidt TS, Bochenek ML, Sakakibara A, et al. Ephrin-B2 controls VEGF-induced angiogenesis and lymphangiogenesis. Nature. 2010;465(7297):483-6.

59. Madisen L, Zwingman TA, Sunkin SM, Oh SW, Zariwala HA, Gu H, et al. A robust and high-throughput Cre reporting and characterization system for the whole mouse brain. Nat Neurosci. 2010;13(1):133-40.
60. Hao Y, Hao S, Andersen-Nissen E, Mauck WM, 3rd, Zheng S, Butler A, et al. Integrated analysis of multimodal single-cell data. Cell. 2021;184(13):3573-87.e29.
61. McGinnis CS, Murrow LM, Gartner ZJ. DoubletFinder: Doublet Detection in Single-Cell RNA Sequencing Data Using Artificial Nearest Neighbors. Cell Systems. 2019;8(4):329-37.e4.
62. Korsunsky I, Millard N, Fan J, Slowikowski K, Zhang F, Wei K, et al. Fast, sensitive and accurate integration of single-cell data with Harmony. Nature Methods. 2019;16(12):1289-96.
63. Zhu A, Ibrahim JG, Love MI. Heavy-tailed prior distributions for sequence count data: removing the noise and preserving large differences. Bioinformatics. 2018;35(12):2084-92.
64. Wu T, Hu E, Xu S, Chen M, Guo P, Dai Z, et al. clusterProfiler 4.0: A universal enrichment tool for interpreting omics data. The Innovation. 2021;2(3).
65. Ieronimakis N, Balasundaram G, Reyes M. Direct isolation, culture and transplant of mouse skeletal muscle derived endothelial cells with angiogenic potential. PLoS One. 2008;3(3):e0001753.

Figure Legends

Figure 1. Single-Cell RNA sequencing reveals cellular heterogeneity in the muscle regenerating niche of Clodronate-treated (CLL) and Control (SHAM) mice

(A) t-SNE embedding of both experimental conditions (Clodronate-treated (CLL) and Control (SHAM)) coloured by individual cluster identities and manually annotated based on canonical skeletal muscle marker gene expression

(B) DotPlot demonstrating cell-type marker gene expression used for meta-cluster classification. Dot size indicates the percentage of cells expressing each gene, and dot colour represents the average expression level.

(C) UMAP embedding of all sequenced samples

(D) Relative proportion and frequency of cell types per experimental condition.

Figure 2. Impact of the defective muscle regenerative microenvironment driven by compromised MP infiltration on MuSCs and FAPs subsets.

(A) Violin Plot showing normalized and log-transformed expression of MuSCs subpopulations specific genes

(B) UMAP plot of MuSCs subclustering split per experimental condition

(C) Relative proportion of MuSCs subpopulations per experimental condition.

(D) UMAP embedding of FAP population split per experimental condition

(E) BarPlot showing selected GO biological process and KEGG-terms gene set enrichment analysis (GSEA) comparing CLL vs SHAM conditions, in FAPs. The Normalized Enrichment Score (NES) indicates the degree of enrichment for each gene set. Positive NES values (in red) represent pathways activated in CLL, while negative NES values (in blue) represent pathways suppressed in CLL.

Figure 3. Impaired MP recruitment results in endothelial cells undergoing transcriptional and phenotypic changes in regenerating muscles.

(A) BarPlot showing the top dysregulated processes from the Gene set enrichment analysis (GSEA) (GO biological process) related to immune response, ECM and endothelial functions in ECs from CLL treated mice. The Normalized Enrichment Score (NES) indicates the degree of enrichment for each gene set. Positive NES values (in red) represent pathways activated in CLL, while negative NES values (in blue) represent pathways suppressed in CLL.

(B) BarPlot showing the dysregulated pathways from the GSEA (KEGG database) in ECs from CLL treated mice. The Normalized Enrichment Score (NES) indicates the degree of enrichment for each gene set. Positive NES values (in red) represent pathways activated in CLL, while negative NES values (in blue) represent pathways suppressed in CLL.

(C) Heatmap showing the expression of the Top 20 differentially expressed genes (DEG) of the 3626 DE genes assessed by DEseq2, $P < 0.05$. Bold genes are related to ECM turnover.

(D) Heatmap of the main endothelial, mesenchymal, EndMT related genes and ECs-MuSCs crosstalk, differentially expressed between conditions.

(E) Immunofluorescence staining of quadriceps muscle cross-sections of SHAM- and CLL-treated Cdh5-CreERT2:R26R-tdTomato mice 5 days post cardiotoxin injury for ECs (CD31, white), tdTomato (green), Col1a1 (red) and nuclear marker (DAPI, blue). White arrows indicate examples of $CD31^+$ or $tdTomato^+$ cells expressing Col1a1. Magnification 40x, Scale bar at 20 μm and amplified images at 8 μm.

(F) Quantification of $CD31^+$ and $CD31^-/tdTomado^+$ cells per square millimetre in quadriceps muscle cross-sections of SHAM- and CLL-treated Cdh5-CreERT2:R26R-tdTomato mice 5 days post cardiotoxin injury (n=3, with three representative sections of the muscle examined). Statistically significant differences are indicated as $***$ representing $P < 0.001$, $CD31^+$ $P=0.0902$ (two-tailed unpaired Student's t-test).

(G) Quantification of $CD31^+/Col1a1^+$ and $tdTomado^+/Col1a1^+$ cells per square millimetre in quadriceps muscle cross-sections of SHAM- and CLL-treated Cdh5-CreERT2:R26R-tdTomato mice 5 days post cardiotoxin injury (n=3, with three representative sections of each muscle examined). Statistically significant differences are indicated as $*$ representing $P < 0.05$ (two-tailed unpaired Student's t-test).

Figure 4. Transcriptomic analysis of MPs in the muscle regenerating niche reveals dysregulated profiles upon compromised MP infiltration

(A) UMAP plot of MPs sub-clustering.

(B) Labelling of cells based on the top expressed marker genes.

(C) DotPlot of the top 5 expressed genes for each sub-cluster and FeaturePlot showing the normalized expression of M2- like specific genes Mrc1 (Cd206), Cd163 and Gpnmb to highlight the sub-clustering of MPs. Dot size indicates the percentage of cells expressing each gene, and dot colour represents the average expression level.

(D) Relative proportion of MP subpopulations per condition.

(E) Visualization by a Volcano plot of the statistically significant gene expression changes (fold change ≥ 1.5 and adjusted P value <0.05) of M2-like MPs between conditions. Upregulated genes are labelled in red and downregulated genes labelled in blue.

(F) BarPlot showing selected GO biological process and KEGG-terms gene set enrichment analysis (GSEA) comparing CLL vs SHAM conditions, in M2-like MPs. The Normalized Enrichment Score (NES) indicates the degree of enrichment for each gene set. Positive NES values (in red) represent pathways activated in CLL, while negative NES values (in blue) represent pathways suppressed in CLL.

Figure 5. Analysis of MP-EC signalling interactions in regenerating muscle.

(A) Chord diagram of MPs and ECs interactions.

(B) Bubble plot showing all the significant interactions between MPs ligands and ECs receptors in both conditions.

(C) Immunofluorescence staining of quadriceps muscle cross-sections of SHAM- and CLL-treated Cdh5-CreERT2:R26R-tdTomato mice 5 days post cardiotoxin injury for MPs (F4/80, red), osteopontin (SPP1, green) and nuclear marker (DAPI, blue). White arrows indicate examples of Macrophages expressing SPP1. Magnification 40x, Scale bar at 20 μm and amplified images at 8 μm.

(D) Quantification of $F4/80^+$ cells per square millimetre in quadriceps muscle cross-sections of SHAM- and CLL-treated Cdh5-CreERT2:R26R-tdTomato mice 5 days post cardiotoxin injury (n=3, with three representative sections of each muscle examined). P=0,0940 (two-tailed unpaired Student's t-test).

(E) Frequency (in %) of $SPP1^+$ macrophages from quadriceps muscle cross-sections of SHAM- and CLL-treated Cdh5-CreERT2:R26R-tdTomato mice 5 days post cardiotoxin injury (n=3, with three representative sections of each muscle examined). Statistically significant difference is indicated as ∗ representing $P < 0.05$ (two-tailed unpaired Student's t-test).

(F) Violin Plot showing the expression of the different TGF-β isoforms, Tnf, Gdf15 and SPP1 on MPs, FAPs, MuSCs, ECs and myocyte populations between conditions.

Figure 6. TGF-β and SPP1 synergize to induce EndMT in mouse skeletal muscle ECs.

(A) mECs at day 0 and day 5, in the different experimental conditions: Control (CT), TGF-β, SPP1, SPP1+TGF-β.

(B) Relative gene expression levels of endothelial and mesenchymal markers of CT, TGF-β, SPP1, SPP1+TGF-β treated mECs. Results are normalized to GAPDH. Data is presented as mean ± SEM (n=3). Statistically significant differences are indicated as ∗, ∗∗, ∗∗∗ and ∗∗∗∗ representing $P < 0.05$, $P < 0.01$, $P < 0.001$ and $P < 0.0001$, respectively (two-tailed unpaired Student's t-test).

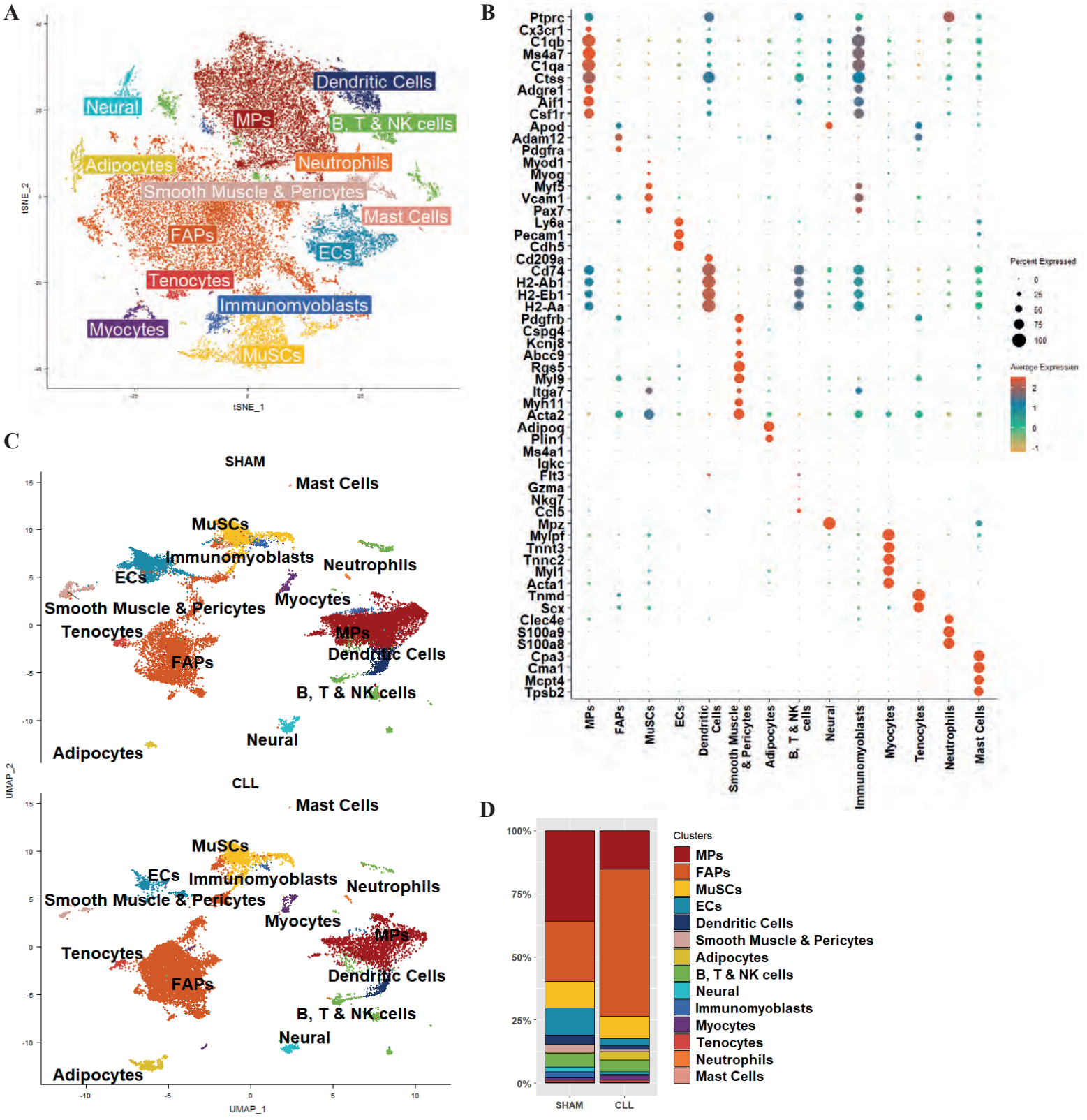

A
Neural
Dendritic Cells
MPs
B, T & NK cells
Adipocytes
Neutrophils
Smooth Muscle & Pericytes
Mast Cells
FAPs
ECs
Tenocytes
Immunomyoblasts
Myocytes
MuSCs
tSNE_1
tSNE_2
B
Ptprc
Cx3cr1
C1qb
Ms4a7
C1qa
Ctss
Adgre1
Aif1
Csf1r
Apod
Adam12
Pdgfra
Myod1
Myog
Myf5
Vcam1
Pax7
Ly6a
Pecam1
Cdh5
Cd209a
Cd74
H2-Ab1
H2-Eb1
H2-Aa
Pdgfrb
Cspg4
Kcnj8
Abcc9
Rgs5
Myl9
Itga7
Myh11
Acta2
Adipoq
Plin1
Ms4a1
Igkc
Flt3
Gzma
Nkg7
Ccl5
Mpz
Mylpf
Tnnt3
Tnnc2
Myl1
Acta1
Tnmd
Scx
Clec4e
S100a9
S100a8
Cpa3
Cma1
Mcpt4
Tpsb2
MPs
FAPs
MuSCs
ECs
Dendritic Cells
Smooth Muscle & Pericytes
Adipocytes
B, T & NK cells
Neural
Immunomyoblasts
Myocytes
Tenocytes
Neutrophils
Mast Cells
Percent Expressed
0
25
50
75
100
Average Expression
2
1
0
-1
C
SHAM
Mast Cells
MuSCs
Immunomyoblasts
Neutrophils
ECs
Myocytes
Smooth Muscle & Pericytes
Tenocytes
MPs
Dendritic Cells
FAPs
B, T & NK cells
Neural
Adipocytes
CLL
Mast Cells
MuSCs
ECs
Immunomyoblasts
Neutrophils
Smooth Muscle & Pericytes
Myocytes
MPs
Tenocytes
Dendritic Cells
FAPs
B, T & NK cells
Neural
Adipocytes
UMAP_1
UMAP_2
D
100%
75%
50%
25%
0%
SHAM
CLL
Clusters
MPs
FAPs
MuSCs
ECs
Dendritic Cells
Smooth Muscle & Pericytes
Adipocytes
B, T & NK cells
Neural
Immunomyoblasts
Myocytes
Tenocytes
Neutrophils
Mast Cells

Figure 1

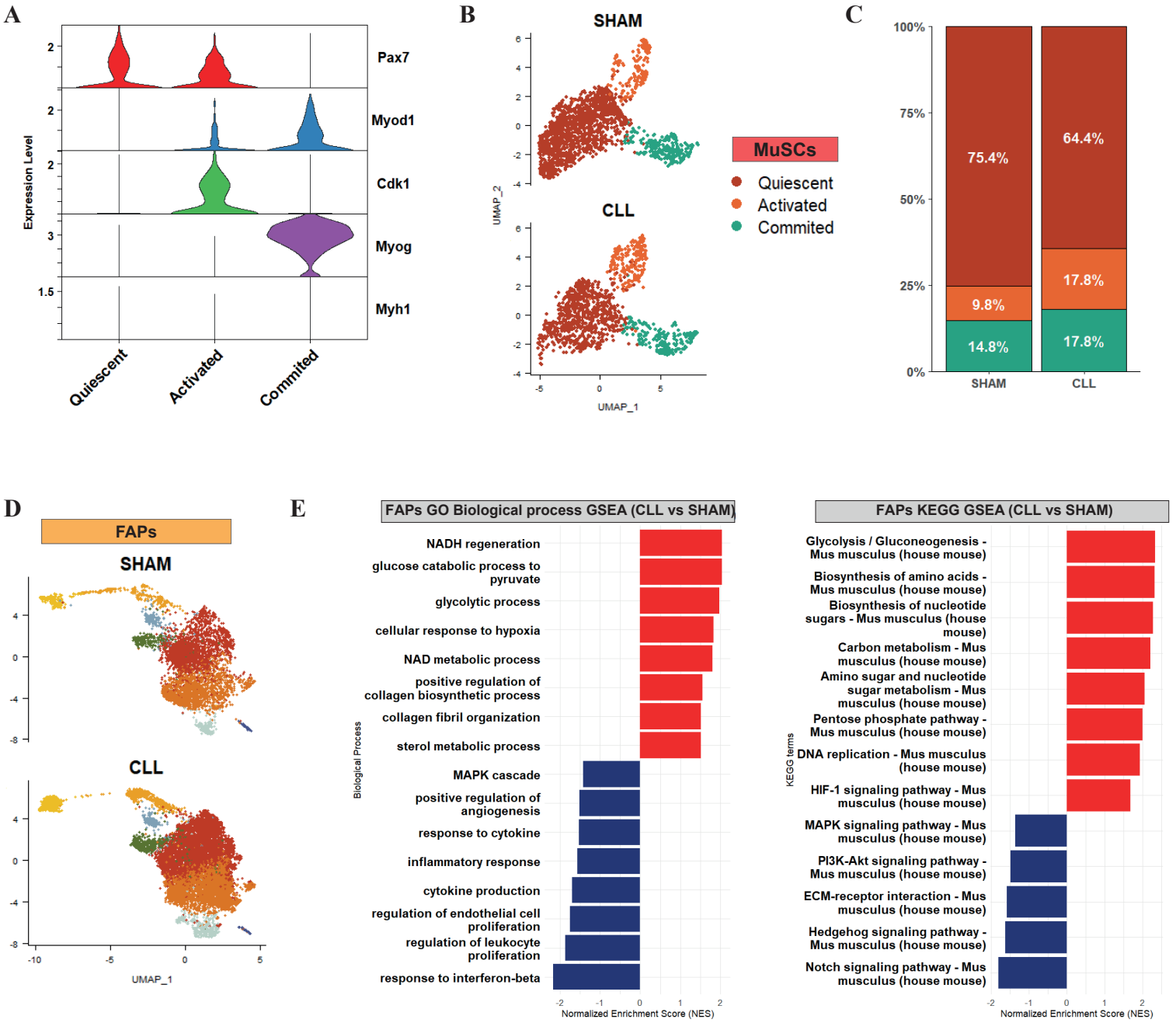

A
Pax7
Myod1
Cdk1
Myog
Myh1
Expression Level
Quiescent
Activated
Commited
B
SHAM
CLL
UMAP_1
UMAP_2
MuSCs
Quiescent
Activated
Commited
C
100%
75%
50%
25%
0%
75.4%
9.8%
14.8%
64.4%
17.8%
17.8%
SHAM
CLL
D
FAPs
SHAM
CLL
UMAP_1
UMAP_2
E
FAPs GO Biological process GSEA (CLL vs SHAM)
NADH regeneration
glucose catabolic process to pyruvate
glycolytic process
cellular response to hypoxia
NAD metabolic process
positive regulation of collagen biosynthetic process
collagen fibril organization
sterol metabolic process
MAPK cascade
positive regulation of angiogenesis
response to cytokine
inflammatory response
cytokine production
regulation of endothelial cell proliferation
regulation of leukocyte proliferation
response to interferon-beta
Biological Process
Normalized Enrichment Score (NES)
FAPs KEGG GSEA (CLL vs SHAM)
Glycolysis / Gluconeogenesis - Mus musculus (house mouse)
Biosynthesis of amino acids - Mus musculus (house mouse)
Biosynthesis of nucleotide sugars - Mus musculus (house mouse)
Carbon metabolism - Mus musculus (house mouse)
Amino sugar and nucleotide sugar metabolism - Mus musculus (house mouse)
Pentose phosphate pathway - Mus musculus (house mouse)
DNA replication - Mus musculus (house mouse)
HIF-1 signaling pathway - Mus musculus (house mouse)
MAPK signaling pathway - Mus musculus (house mouse)
PI3K-Akt signaling pathway - Mus musculus (house mouse)
ECM-receptor interaction - Mus musculus (house mouse)
Hedgehog signaling pathway - Mus musculus (house mouse)
Notch signaling pathway - Mus musculus (house mouse)
KEGG terms
Normalized Enrichment Score (NES)

Figure 2

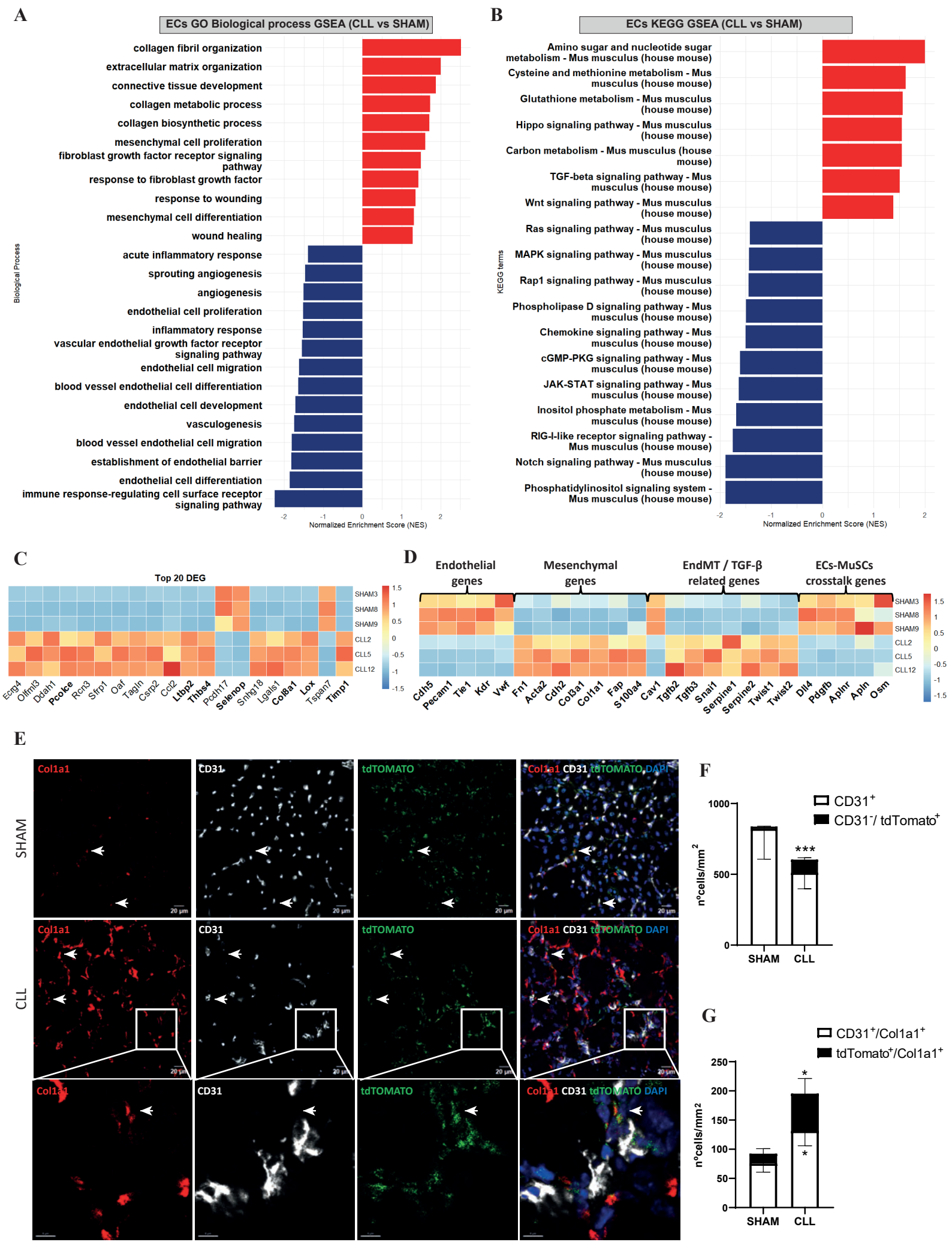

A
ECs GO Biological process GSEA (CLL vs SHAM)
collagen fibril organization
extracellular matrix organization
connective tissue development
collagen metabolic process
collagen biosynthetic process
mesenchymal cell proliferation
fibroblast growth factor receptor signaling pathway
response to fibroblast growth factor
response to wounding
mesenchymal cell differentiation
wound healing
acute inflammatory response
sprouting angiogenesis
angiogenesis
endothelial cell proliferation
inflammatory response
vascular endothelial growth factor receptor signaling pathway
endothelial cell migration
blood vessel endothelial cell differentiation
endothelial cell development
vasculogenesis
blood vessel endothelial cell migration
establishment of endothelial barrier
endothelial cell differentiation
immune response-regulating cell surface receptor signaling pathway
Biological Process
-2 -1 0 1 2
Normalized Enrichment Score (NES)
B
ECs KEGG GSEA (CLL vs SHAM)
Amino sugar and nucleotide sugar metabolism - Mus musculus (house mouse)
Cysteine and methionine metabolism - Mus musculus (house mouse)
Glutathione metabolism - Mus musculus (house mouse)
Hippo signaling pathway - Mus musculus (house mouse)
Carbon metabolism - Mus musculus (house mouse)
TGF-beta signaling pathway - Mus musculus (house mouse)
Wnt signaling pathway - Mus musculus (house mouse)
Ras signaling pathway - Mus musculus (house mouse)
MAPK signaling pathway - Mus musculus (house mouse)
Rap1 signaling pathway - Mus musculus (house mouse)
Phospholipase D signaling pathway - Mus musculus (house mouse)
Chemokine signaling pathway - Mus musculus (house mouse)
cGMP-PKG signaling pathway - Mus musculus (house mouse)
JAK-STAT signaling pathway - Mus musculus (house mouse)
Inositol phosphate metabolism - Mus musculus (house mouse)
RIG-I-like receptor signaling pathway - Mus musculus (house mouse)
Notch signaling pathway - Mus musculus (house mouse)
Phosphatidylinositol signaling system - Mus musculus (house mouse)
KEGG terms
-2 -1 0 1 2
Normalized Enrichment Score (NES)
C
Top 20 DEG
SHAM3
SHAM8
SHAM9
CLL2
CLL5
CLL12
1.5 1 0.5 0 -0.5 -1 -1.5
Edrg4 Olfml3 Ddah1 Pcolce Rcn3 Sfrp1 Oaf Tagln Csrp2 Col2 Ltbp2 Thbs4 Pcdh17 Selenop Snhg18 Lgals1 Col8a1 Lox Tspan7 Timp1
D
Endothelial genes
Mesenchymal genes
EndMT / TGF-β related genes
ECs-MuSCs crosstalk genes
SHAM3
SHAM8
SHAM9
CLL2
CLL5
CLL12
1.5 1 0.5 0 -0.5 -1 -1.5
Cdh5 Pecam1 Tie1 Kdr Vwf Fn1 Acta2 Cdh2 Col3a1 Col1a1 Fap S100a4 Cav1 Tgfb2 Tgfb3 Snai1 Serpine1 Serpine2 Twist1 Twist2 Dll4 Pdgfb Apln Aplnr Osm
E
SHAM
CLL
Col1a1
CD31
tdTOMATO
Col1a1 CD31 tdTOMATO DAPI
20 µm
F
CD31+
CD31-/ tdTomato+
n°cells/mm2
1000
500
0
***
SHAM
CLL
G
CD31+/Col1a1+
tdTomato+/Col1a1+
n°cells/mm2
250
200
150
100
50
0
*
*
SHAM
CLL

Figure 3

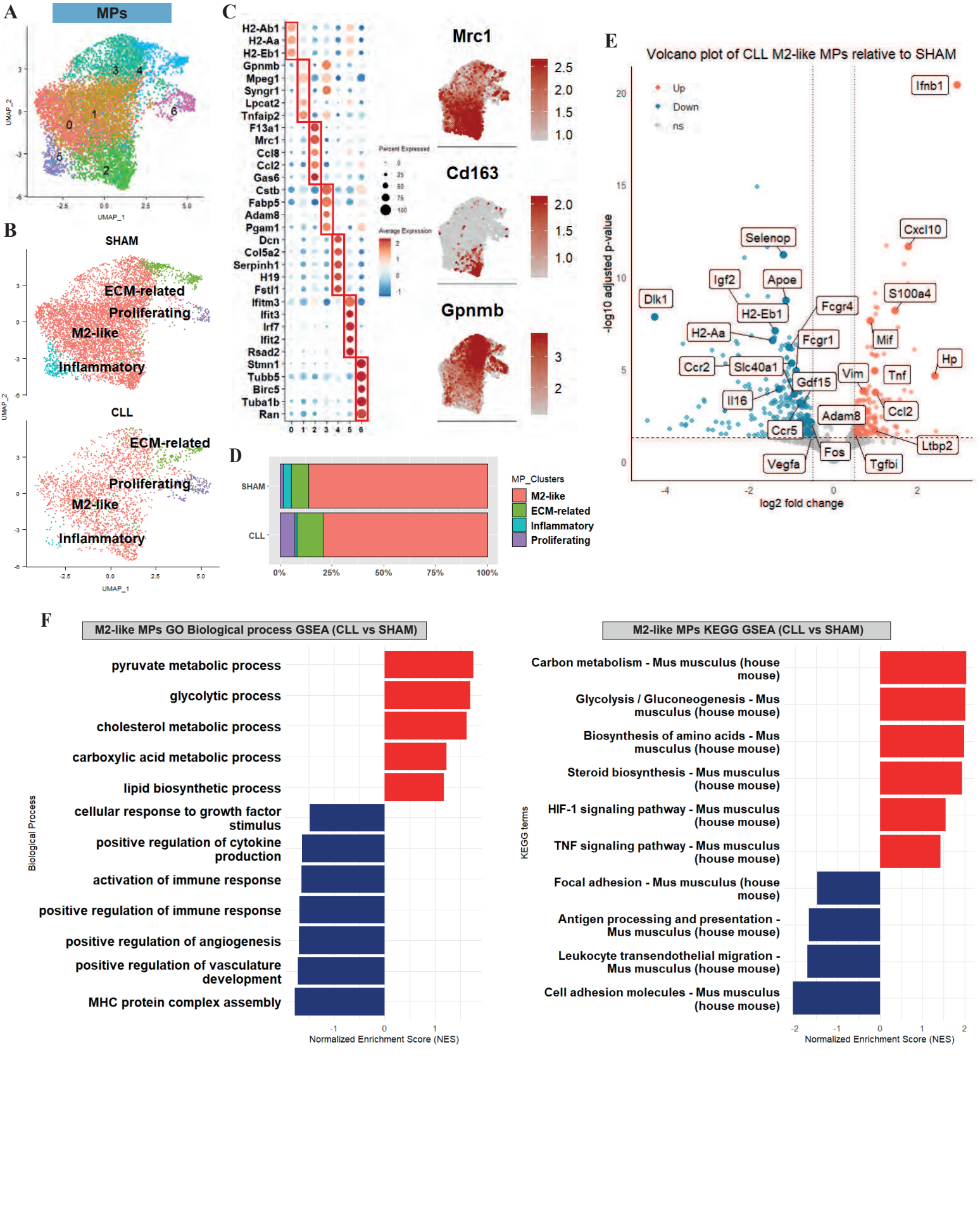

A
MPs
UMAP_1
UMAP_2
B
SHAM
ECM-related
Proliferating
M2-like
Inflammatory
CLL
C
H2-Ab1
H2-Aa
H2-Eb1
Gpnmb
Mpeg1
Syngr1
Lpcat2
Tnfaip2
F13a1
Mrc1
Ccl8
Ccl2
Gas6
Cstb
Fabp5
Adam8
Pgam1
Dcn
Col5a2
Serpinh1
H19
Fstl1
Ifitm3
Ifit3
Irf7
Ifit2
Rsad2
Stmn1
Tubb5
Birc5
Tuba1b
Ran
Percent Expressed
Average Expression
Mrc1
Cd163
Gpnmb
D
SHAM
CLL
MP_Clusters
M2-like
ECM-related
Inflammatory
Proliferating
E
Volcano plot of CLL M2-like MPs relative to SHAM
Up
Down
ns
-log10 adjusted p-value
log2 fold change
Ifnb1
Cxcl10
Selenop
Igf2
Apoe
Dlk1
S100a4
Fcgr4
H2-Eb1
H2-Aa
Fcgr1
Mif
Hp
Ccr2
Slc40a1
Vim
Tnf
Gdf15
Il16
Ccl2
Adam8
Ccr5
Ltbp2
Fos
Vegfa
Tgfbi
F
M2-like MPs GO Biological process GSEA (CLL vs SHAM)
pyruvate metabolic process
glycolytic process
cholesterol metabolic process
carboxylic acid metabolic process
lipid biosynthetic process
cellular response to growth factor stimulus
positive regulation of cytokine production
activation of immune response
positive regulation of immune response
positive regulation of angiogenesis
positive regulation of vasculature development
MHC protein complex assembly
Biological Process
Normalized Enrichment Score (NES)
M2-like MPs KEGG GSEA (CLL vs SHAM)
Carbon metabolism - Mus musculus (house mouse)
Glycolysis / Gluconeogenesis - Mus musculus (house mouse)
Biosynthesis of amino acids - Mus musculus (house mouse)
Steroid biosynthesis - Mus musculus (house mouse)
HIF-1 signaling pathway - Mus musculus (house mouse)
TNF signaling pathway - Mus musculus (house mouse)
Focal adhesion - Mus musculus (house mouse)
Antigen processing and presentation - Mus musculus (house mouse)
Leukocyte transendothelial migration - Mus musculus (house mouse)
Cell adhesion molecules - Mus musculus (house mouse)
KEGG terms
Normalized Enrichment Score (NES)

Figure 4

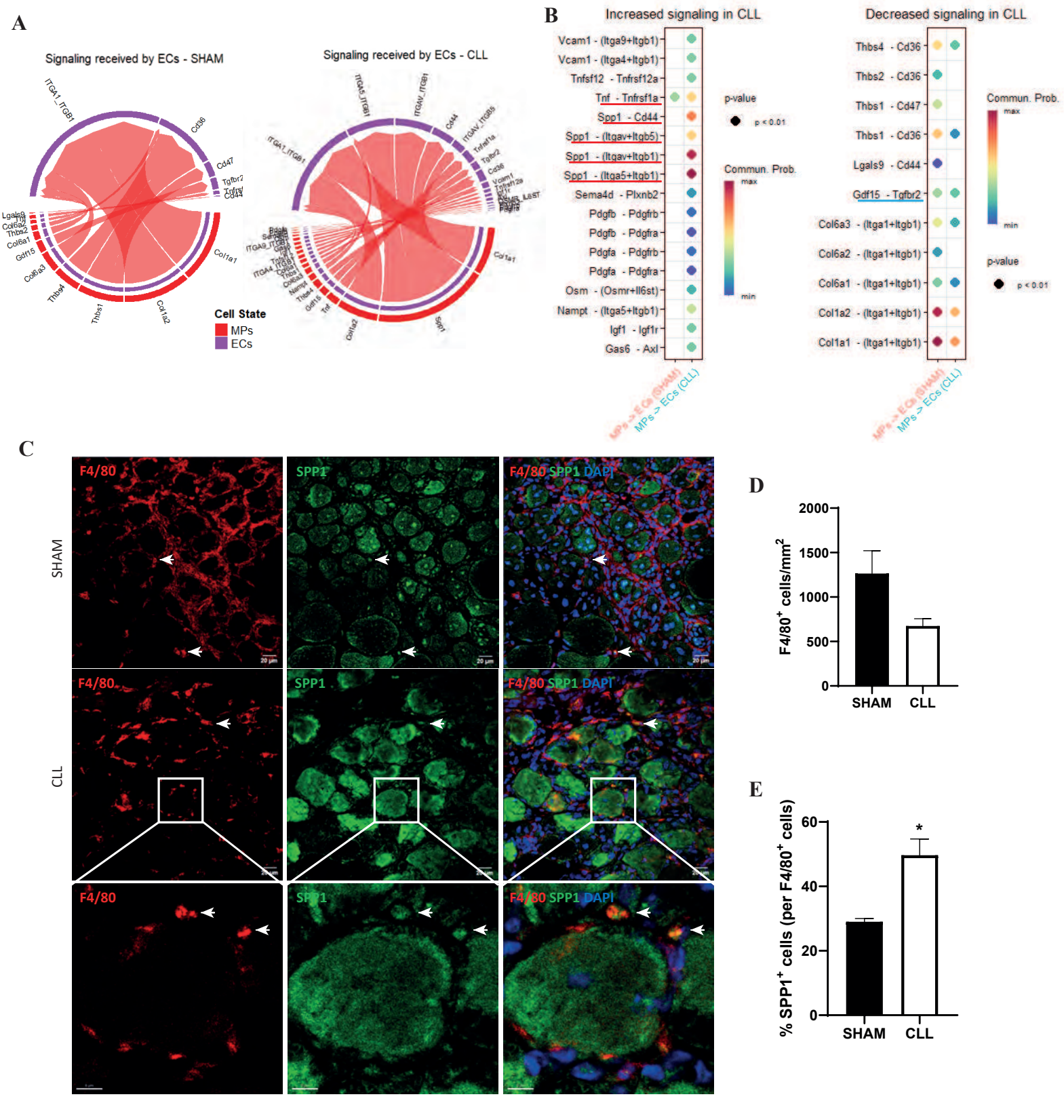

A
Signaling received by ECs - SHAM
Signaling received by ECs - CLL
Cell State
MPs
ECs
B
Increased signaling in CLL
Decreased signaling in CLL
Vcam1 - (Itga9+Itgb1)
Vcam1 - (Itga4+Itgb1)
Tnfsf12 - Tnfrsf12a
Tnf - Tnfrsf1a
Spp1 - Cd44
Spp1 - (Itgav+Itgb5)
Spp1 - (Itgav+Itgb1)
Spp1 - (Itga5+Itgb1)
Sema4d - Plxnb2
Pdgfb - Pdgfrb
Pdgfb - Pdgfra
Pdgfa - Pdgfrb
Pdgfa - Pdgfra
Osm - (Osmr+Il6st)
Nampt - (Itga5+Itgb1)
Igf1 - Igf1r
Gas6 - Axl
Thbs4 - Cd36
Thbs2 - Cd36
Thbs1 - Cd47
Thbs1 - Cd36
Lgals9 - Cd44
Gdf15 - Tgfbr2
Col6a3 - (Itga1+Itgb1)
Col6a2 - (Itga1+Itgb1)
Col6a1 - (Itga1+Itgb1)
Col1a2 - (Itga1+Itgb1)
Col1a1 - (Itga1+Itgb1)
p-value
p < 0.01
Commun. Prob.
max
min
MPs -> ECs (SHAM)
MPs -> ECs (CLL)
C
SHAM
CLL
F4/80
SPP1
F4/80 SPP1 DAPI
D
F4/80+ cells/mm2
2000
1500
1000
500
0
SHAM
CLL
E
% SPP1+ cells (per F4/80+ cells)
60
40
20
0
*
SHAM
CLL
F
Expression Level
Spp1
Gdf15
Tnf
Tgfb1
Tgfb2
Tgfb3
MPs
FAPs
MuSCs
ECs
Myocytes
SHAM
CLL

Figure 5

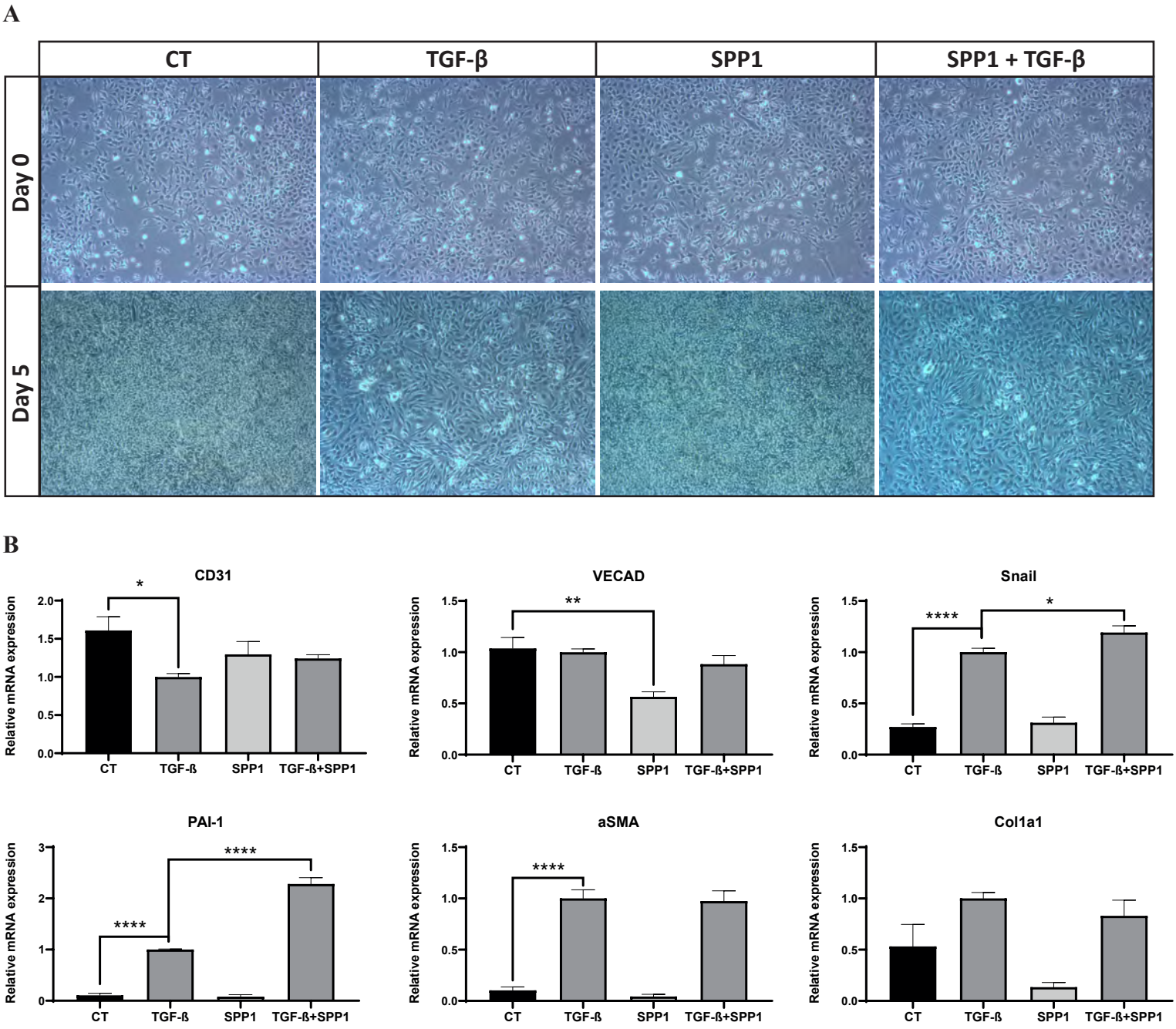

A
CT
TGF-β
SPP1
SPP1 + TGF-β
Day 0
Day 5
B
CD31
VECAD
Snail
PAI-1
aSMA
Col1a1
Relative mRNA expression
CT
TGF-ß
SPP1
TGF-ß+SPP1

Figure 6

Supplementary Files

This is a list of supplementary files associated with this preprint. Click to download.

- Supplementarytable2gseaFAPs.xlsx
- Supplementarytable4gseaECs.xlsx
- Supplementarytable6gseaM2MPs.xlsx
- Supplementarytable5DEGM2MPs.xlsx
- Supplementarytable1DEGFAPs.xlsx
- SupplementaryTable3DEGECs.xlsx
- Supplementarytable7cellchat.xlsx
- FerreiraSupplementaryfiguresred.pdf
- RS1233.pdf